STRUCTURAL, TRANSPORT AND MAGNETIC PROPERTIES OF $(Fe_{100-x}V_x)_{75}P_{15}C_{10}$ AMORPHOUS RIBBONS

A Thesis Submitted to the Department of Physics, Bangladesh University of Engineering and Technology, Dhaka in Partial Fulfillment of the Requirement for the Degree of Master of Philosophy in Physics

SUBMITTED BY

MOHAMMAD ABU SAYEM KARAL

ROLL NO.: 040814005P

SESSION: April 2008

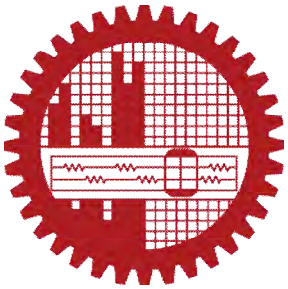

DEPARTMENT OF PHYSICS
BANGLADESH UNIVERSITY OF ENGINEERING &TECHNOLOGY
DHAKA-1000, BANGLADESH

BANGLADESH UNIVERSITY OF ENGINEERING AND TECHNOLOGY

DEPARTMENT OF PHYSICS, DHAKA-1000

Certification of thesis work

The thesis titled **"STRUCTURAL, TRANSPORT AND MAGNETIC PROPERTIES OF $(Fe_{100-x}V_x)_{75}P_{15}C_{10}$ AMORPHOUS RIBBONS",** submitted by **MOHAMMAD ABU SAYEM KARAL**, Roll No.: 040814005 P, Session: April-2008, has been accepted as satisfactory in partial fulfillment of the requirement for the degree of Master of Philosophy (M. Phil.) in Physics on June 14, 2011.

BOARD OF EXAMINERS

1. _____
   DR. MD. FEROZ ALAM KHAN (Supervisor) — Chairman
   Professor, Department of Physics
   BUET, Dhaka-1000

2. _____
   DR. A. K. M. AKTHER HOSSAIN — Member (Ex-officio)
   Professor & Head, Department of Physics
   BUET, Dhaka-1000

3. _____
   DR. JIBAN PODDER — Member
   Professor, Department of Physics
   BUET, Dhaka-1000

4. _____
   DR. GOLAM MOHAMMAD BHUIYAN — Member (External)
   Professor, Department of Theoretical Physics
   University of Dhaka, Dhaka-1000

CANDIDATE'S DECLARATION

It is hereby declared that this thesis or any part of it has not been submitted elsewhere for the award of any degree or diploma.

MOHAMMAD ABU SAYEM KARAL

DEDICATED

TO

MY BOLOVED PARENTS

ACKNOWLEDGEMENTS

In preparation of this thesis, I must acknowledge the contributions of many people in various ways.

Firstly, the most significant contribution for which I shall remain grateful to my supervisor Professor Dr. Md. Feroz Alam Khan, Department of Physics, Bangladesh University of Engineering and Technology (BUET), Dhaka for his supervision, constant guidance, untold patience, valuable suggestions and inspiration that helped me to complete this thesis work in its present form.

Secondly, I would like to express my sincere thanks to Professor Dr. A. K. M Akther Hossain, Head, Department of Physics, BUET for his valuable suggestions and inspirations to complete the thesis.

Thirdly, I would like to express my cordial thanks to all respected teachers of the Department of Physics, BUET specially Professor Dr. Md. Abu Hashan Bhuiyan, Professor Dr. Nazma Zaman, Professor Dr. Jiban Poddar, Professor Dr. Md. Mostak Hossain, Mrs. Fahima Khanom, Dr. Afia Begum, Dr. Md. Rafi Uddin, Dr. Nasren Akther, Dr. Md. Forhad Mina, M. Abdul Basith, M. Rakibul Islam, M. Samir Ullah, M. Jellur Rahman, M. Khurshed Alam, M. Azizar Rahman, Mahabub Alam Bhuiyan, Rabeya Ferdousi for their encouragement and help during my research work.

In addition to, I would like express my sincere thanks to M. Kamruzzaman, an M. Phil student of the Department of Physics, BUET for his assistance during my experimental work. I am also thankful to Md. Idris Munsi, Assistant Technical officer of the Department of Physics for his sincere help and cooperation during the thesis work. Thanks are also due to all staff of the Department of Physics, BUET for giving necessary support to my research work. I would also like to thank Dr. Dilip Kumer Shah, Chief Scientific Officer, Atomic Energy Centre, Dhaka Bangladesh for providing the XRD measurements of this research work.

Moreover, I would mention a very special gratefulness for the moral support and sustaining inspiration provided by the members of my family specially my wife and my daughter. This thesis would never have been possible without their love, affection and encouragement.

Furthermore, I would like to express my gratefulness to the authority of BUET for giving me the opportunity to do this research work and financial support. I am thankful to the International Programme for Physical Sciences (IPPS) for providing extensive instruments to the Department of Physics, BUET which are used in this work.

Finally, I would like to express my heartfelt gratitude to Almighty Allah whose mercy helped me all time.

ABSTRACT

Structural, thermal, transport and magnetic properties of $(Fe_{100-x}V_x)_{75}P_{15}C_{10}$ (x=0, 5, 10 and 15) amorphous ribbons prepared by melt spinning technique were studied. The XRD of the as prepared samples shows a broad peak that confirms the samples are in amorphous nature. The re-crystallization phenomenon of the alloys was studied by XRD for annealing temperatures from 400 to 650 °C for 30 minutes annealing time. The XRD pattern shows that all compositions remain in the b.c.c phase within the annealing temperature range between 400 and 450 °C, and transform into hexagonal phase within the annealing temperature range between 500 and 650 °C. The lattice parameter 'a' of the b.c.c structure changes from 2.854 to 2.870 Å. The lattice parameters 'a' and 'c' of the hexagonal structure are (5.011-5.045) Å and (13.676-13.822) Å, respectively. The grain size is found to vary from 10 to 60 nm depending on the annealing temperature. The DTA curves of the as prepared samples show an exothermic peak for each sample. The crystallization temperatures increase with the increases of V content. Surface micrograph of the as prepared samples shows that porosity decreases with the increase of V content. The resistivity at room temperature of the as prepared samples increases with the increase of V content and attributed to the isotropic, anisotropic and topological scattering of the conduction electrons. The resistivity of the as prepared samples follows Mooij-correlation in the temperature range 298-93K. The magnetoresistance of the as prepared samples vary from 0 to 8% which is typical of metallic glass system. The origin of magnetoresistance is assumed to be magnon-electron and/or phonon-electron interaction. Room temperature Hall resistivity of the as prepared samples show anomalous Hall effect due to the impurity, phonon and spin disorder scattering. The skew-scattering and the side-jump mechanism are also responsible for anomalous Hall effect. Room temperature saturation magnetization of the as prepared samples decreases with the increase of V content. This decrease is due to the replacement of ferromagnetic Fe by paramagnetic V and also due to the reduction of the overall interatomic exchange interaction.

LIST OF FIGURES

Chapter-5

LIST OF TABLES

LIST OF SYMBOLS AND ABBREVIATIONS

Fe	-	Iron
V	-	Vanadium
P	-	Phosphorus
C	-	Carbon
Cu	-	Copper
Nb	-	Niobium
Ta	-	Tantalum
Si	-	Silicon
B	-	Boron
Co	-	Cobalt
Mn	-	Manganese
RT	-	Room temperature
$\rho(RT)$	-	Resistivity at room temperature.
$\rho(T)$	-	Resistivity at any temperature
$\frac{\rho(T)}{\rho(RT)}$	-	Normalized resistivity
MR%	-	Magnetoresistance in percentage
R	-	Resistance
X	-	Reactance
L_{ex}	-	Exchange interaction length
H_c	-	Coercivity
E_k	-	Anisotropy energy
M_s	-	Saturation magnetization
μ_B	-	Bohr magneton
T_C	-	Curie temperature
T_g	-	Glass transition temperature
T_x	-	Crystallization temperature
T_m	-	Melting temperature
kG	-	Kilogauss
DTA	-	Differential thermal analysis
TG	-	Thermo gravimetric
DTG	-	Differential thermo gravimetric

DSC	-	Differential scanning calorimetry
XRD	-	X-ray diffraction
SEM	-	Scanning electron microscope
TEM	-	Transmission electron microscope
VSM	-	Vibrating sample magnetometer
TCR	-	Temperature coefficient of resistivity ($=\frac{1}{\rho}\frac{\partial\rho}{\partial T}$)
Θ_D	-	Debye temperature
MHz	-	Megahertz
GHz	-	Gigahertz
SWR	-	Spin wave resonance
FM	-	Ferromagnetic
AFM	-	Anti-ferromagnetic
FMR	-	Ferromagnetic resonance
WB	-	Bloch wall

CONTENTS

STRUCTURAL, TRANSPORT AND MAGNETIC PROPERTIES OF $(Fe_{100-x}V_x)_{75}P_{15}C_{10}$ AMORPHOUS RIBBONS

MOHAMMAD ABU SAYEM KARAL

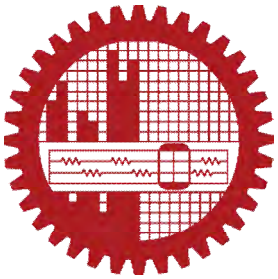

DEPARTMENT OF PHYSICS
BANGLADESH UNIVERSITY OF ENGINEERING &TECHNOLOGY
DHAKA-1000, BANGLADESH
JUNE - 2011

CHAPTER 1
INTRODUCTION

1.1 Introduction

An amorphous material is a material which has disordered atomic structure. In contrast to most metals, that is crystalline in nature and has a highly ordered atomic structure. Amorphous alloys are non-crystalline materials in which disordered structure is produced directly from the liquid state during cooling, and so these materials are commonly referred to as metallic glasses or glassy metals. The first reported metallic glass was an alloy of $Au_{75}Si_{25}$ produced by J. W. Klement et al [1] in 1960. This and other early glass-forming alloys had to be cooled rapidly to avoid crystallization. Metallic glasses could only be produced in a limited number of forms typically ribbons, foils, wires etc. The specimens of metallic glasses were limited to thicknesses of less than one hundred micrometers. In 1976, H. Liebermann et al [2] developed a new method of manufacturing thin ribbons of amorphous metal on a super cooled fast-spinning wheel. This was an alloy of iron, nickel, phosphorus and boron. In the early 1980s, glassy ingots with 5 mm diameter were produced from the alloy of $Pd_{55}Pb_{22.5}Sb_{22.5}$ by surface etching followed with heating-cooling cycles. Using boron oxide flux, the achievable thickness was increased to a centimeter. Metallic glasses have been found to be promising for technological applications in 1988 [3]. There are two technologically important classes of magnetic amorphous alloys; the transition metal-metalloid (TM-M) alloys and the rare earth-transition metal (RE-TM) alloys. The TM-M alloys typically contain about 80 % Fe, Co, or Ni atom with the remaining are B, C, Si, P or Al as glass forming materials. The presence of the metalloids is necessary to lower the melting point, making it possible to quench the alloy through its glass temperature rapidly enough to form the amorphous phase.

Amorphous ferromagnetic material has been a subject of considerable interest in recent years [4]. The present study involves the preparation and characterization of Fe based amorphous ribbons. The melt spinning technique [5] has been used for the preparation of $(Fe_{100-x}V_x)_{75}P_{15}C_{10}$ (x=0, 5, 10 and 15) ribbons. Here Fe has been partially replaced by V content.

The methods of the preparation of the ribbons are described in chapter-3 along with the procedure and conditions for glass forming amorphous materials. In this alloys P and C have been used as glass forming materials. It has received considerable experimental and theoretical attention owing to the structural, transport and magnetic properties. These materials are interesting from both the fundamental and applied viewpoints. Because of various superior mechanical, magnetic and electrical properties, in comparison with those of the crystalline state, metallic glasses form a class of technologically important materials. It has already been put into applications in different devices e.g., choke coils, high frequency transformers and the magnetic thin film heads [6]. The structural property studies of the materials are most important for the explanation of behavior of that material due to engineering and scientific applications. The studies of the magnetic property of amorphous ribbons are significant for a variety of applications such as power generator transformers, magnetic heads, magnetic shielding etc. These applications may be determined by static or dynamic properties of the amorphous material. Generally high electrical resistivity, high mechanical strength, good corrosion resistance, and absence of crystalline anisotropy, structural defects and grain boundaries characterize the amorphous ribbons. The magnetic properties such as saturation flux density, curie temperature, magnetostriction and induced anisotropy can be controlled by the alloy composition and a subsequent heat treatment.

The high electrical resistivity and the small thickness of the melt-quenched ribbons lead to low eddy current losses. The low hysteresis losses and, results in very low core losses, which are of interest for power electronics at high frequencies. For application in small electronic devices, the amorphous ribbons have somewhat poorer losses than the conventional Fe-Ni-B ribbon. The design optimization requires lower cost of amorphous ribbons, higher induction compared to Fe-Ni-B ribbons. Amorphous ribbons have many refined applications also like development of magnetic bubbles for computer memory, amorphous superconductors etc. Research in the theoretical understanding, development and application of amorphous ribbons can thus be profitable, especially at its present new phase.

1.2 Review of the previous work

The rate of crystallization and the behavior of crystallization of an amorphous $Fe_{75}P_{15}C_{10}$ alloy [7, 8] obtained by rapid cooling from the liquid state had been studied by thermal analysis, XRD, electron microscopy and electrical resistivity. The results of these investigations showed that the rate, as well as the morphology of the amorphous to crystalline transformation greatly depends on the rate of heating. At very high rates of heating (above about 300 °C/min) the transformation is very rapid and is accompanied by a large heat release of about of the order of 900 Cal/mole. The results of experiments performed at a relatively small rate of heating of 1 °C/min confirm the more or less discontinuous nature of the process of nucleation and growth of the equilibrium phases. It evidenced by the sudden increase in the peak intensity of the Fe and Fe_3P XRD peaks around 430 °C, which is near the temperature at which sudden crystallization occurs at high rates of heating. A better understanding of the early stages of crystallization were gained by making isothermal aging experiments within the critical temperature range between 340 °C and 460 °C and studied the progress of crystallization over very long periods of time. The experiments indicated that during the initial stages of crystallization, very small crystallites are formed in the amorphous matrix. Transformation of the amorphous $Fe_{75}P_{15}C_{10}$ alloy to the crystalline phases takes place by the nucleation and growth processes. The morphology of crystalline phases consisting of α-iron and Fe_2P in $Fe_{75}P_{15}C_{10}$ alloys first becomes pronounced after annealing at 360 °C. The Fe_3P phase was detected upon annealing between 380 and 400 °C. After a 96 h anneal at 400 °C, Fe_3C was also formed with the micro structure consisting of α-iron, Fe_3P and Fe_3C. At 420°C the above phases were formed and the transformation of amorphous $Fe_{75}P_{15}C_{10}$ alloy to crystalline phases seems to be complete.

The resistivity, magnetoresistance and the Hall resistivity of amorphous $(Fe_{100-x}Mn_x)_{75}P_{15}C_{10}$ alloys [9] upto 30% Mn were measured using amorphous ribbons. The temperature and field dependence of resistivity and Hall resistivity suggest a variety of structural and spin scattering centers; in particular, temperature dependant resistivity to be governed by structural (isotropic) scattering centers while temperature dependant of Hall resistivity dominated by topological (anisotropic) spin scattering centers.

Transport and magnetic properties of amorphous $(Fe_{1-x}Mn_x)_{75}P_{15}C_{10}$ alloys [10] with x=0.05 and x=0.5 showed that zero coercive field H_c for x=0.05 and upper limit $H_c \leq 1.5G$ for x=0.5. The crystallization temperatures were 740 K and 710 K for x=0.5 and x=0.05 respectively. The resistivity was the order of 10^{-6} Ω-m and magnetic moment per cation was 0.42 μ_B. Pressure derivative of the Curie temperature (T_c) [11] showed that T_c decreases with pressure. Thermoelectric power of some $(Fe_{1-x}Mn_x)_{75}P_{15}C_{10}$ amorphous alloys were studied by E. Kraus et al [12]. Variation of x from 0 to 1 changes the magnetic transition from an amorphous ferromagnetic $Fe_{75}P_{15}C_{10}$ to an amorphous antiferromagnetic $Mn_{75}P_{15}C_{10}$ [13, 14].

The electrical resistivity of amorphous and crystalline $Fe_{80-x}V_xB_{14}Si_6$ alloys [15] was studied as a function of temperature between 4 K and 1200 K. The crystallization temperature increases from 681 K for $Fe_{80}B_{14}Si_6$ to 868 K for $Fe_{64}V_{16}B_{14}Si_6$. A minimum resistivity was observed in the amorphous state at low temperature for samples with $4<x<16$; however this behavior could not show the samples in the crystalline state. The values of T_c were changes slightly with increase of V content.

The influence of Fe substitution by V was studied in amorphous and nanocrystalline $Fe_{73.5-x}V_xCu_1Nb_3Si_{13.5}B_9$ alloys on their structure and magnetic properties [16]. Nanocrystalline state of the samples was represented by $Fe(V)_3Si$ nanocrystals with cubic lattice and mean grain size of the crystals was about 15 nm. V increases the crystallization temperature of the $Fe(V)_3Si$ phase. For higher V content ($x \geq 5$) the ferromagnetic exchange interactions between the grains were less efficient and then the coercivity increases and magnetization decreases.

The low temperature resistivity measurement in $Fe_{80}B_{20-x}C_x$ [17] showed a resistivity minimum which increases slightly with an increase in the carbon concentration. The depth of the minimum was also increased with an increase in the carbon concentration. The result suggests strong evidence against the existence of a dominant magnetic contribution to the origin of the resistivity minimum. The low-temperature data of the ribbon samples between 4.2 and 11 K fit better with lnT than $T^{1/2}$. The magnetoresistance data seem to suggest that both localization and correlation effects to be incorporated in describing the effect of a magnetic field on the electrical resistivity.

Experimental results of magnetization and Mossbauer measurements on an amorphous ferromagnetic alloy $Fe_{75}P_{15}C_{10}$ [18] showed that there was a significant magnetization distribution in an amorphous ferromagnet. It was concluded that the magnetic properties such as saturation magnetization and T_c were determined mainly by short-range order and was not significantly affected as a result of losing the long-range structural order. The overall temperature dependence of the magnetization of an amorphous alloy can be qualitatively understood in terms of the spin-wave "impurity" states in ferromagnet, if a distribution of exchange interaction among the magnetic constituents was assumed. A magnetization fluctuation in amorphous alloys was also consistent with the experimental observation of the coexistence of the Kondo-type resistance minimum in ferromagnetism.

1.3 Aim and objective of the research

The aim and objective of the present work is to study the melt spun $(Fe_{100-x}V_x)_{75}P_{15}C_{10}$ (x=0, 5, 10 and 15) amorphous metallic ribbons through structural, thermal, transport, and magnetic properties.

(i) The structure of as the prepared and annealed samples will be studied by XRD.
(ii) DTA, TG% and DTG of the as prepared samples will be done to investigate the crystallization temperature, mass loss/gain and small change of mass with heating temperature respectively.
(iii) Surface micrographs of the as prepared samples will be studied using a scanning electron microscope.
(iv) The resistivity of the as prepared samples will be measured by four-probe technique at room temperature.
(v) The temperature dependent resistivity of the as prepared samples will be carried out in a liquid nitrogen atmosphere in the temperature range 298-93 K.
(vi) Both the magnetoresistance (MR) and the Hall resistivity of the as prepared samples will be carried out at room temperature upto 0.57 T magnetic field.
(vii) DC magnetization of the as prepared samples will be measured at room temperature in a VSM in the presence of magnetic field upto 1.2 kG.

1.4 Organization of the thesis paper

The organization of the thesis paper is as follows:

Chapter-1 deals with a brief overview of materials, importance and aim of the research work.

Chapter-2 gives the theoretical background of the amorphous materials.

Chapter-3 gives the details of the technique of sample preparation.

Chapter-4 describes the experimental part and descriptions of different measurement techniques that has been used in this research work.

Chapter-5 is devoted to the results of various investigations of the study and their interpretation based on the existing theories.

Chapter-6 gives the conclusion of the research work.

References

[1] Klement, J. W., Willens, R. H., and Duwez, P., "Non-crystalline structure in solidified gold-silicon alloys", Nature, 187, 869-870, 1960.

[2] Libermann, H., and Graham, C., "Production of amorphous alloy ribbons and effects of apparatus parameters on ribbon dimensions", IEEE Trans. on Magn., 12(6), 921-923, 1976.

[3] Yoshizawa, Y., Oguma, S. and Yamauchi, K., "New Fe-based soft magnetic alloys composed of ultrafine grain structure", J. Appl. Phys., 64, 6044-6046, 1988.

[4] Amophous Magnetism, edited by H. O. Hopper and A. M. de Graaf, Plenum, New York, 1973.

[5] Budhani, R. C., Goel, T. C., and Chopra, K. L., "Melt spinning technique for preparation of metallic glasses", Bull. Mater. Sci., 4(5), 549-561, 1982.

[6] Yoshizawa, Y., and Yamauchi, K., "Magnetic properties of Fe-Cu-M-Si-B (M = Cr, V,. Mo, Nb, Ta, W) alloys", Mater Sci. Eng. A, 133, 176-179, 1991.

[7] Rastogi, P. K., and Duwez, P., "Rate of crystallization of an amorphous Fe-P-C alloy", J. Non-crystalline solids, 5, 1-16, 1970.

[8] Rastogi, P. K., "Crystallization behavior of an amorphous Fe-P-C alloy", J. Mat. Sci. Lett., 8, 140-143, 1973.

[9] Heinemann, K., Barner, K., "Transport properties of magnetically ordered amorphous $(Fe_{100-x}Mn_x)_{75}P_{15}C_{10}$ alloys", J. Magn. Magn. Mater., 80, 257-264, 1989.

[10] Heinemann, K., and Barner, K., "Transport and magnetic properties of amorphous $(Fe_{1-x}Mn_x)_{75}P_{15}C_{10}$ alloys", J. Magn. Magn. Mater., 42, 291-294, 1984 .

[11] Medvedeva, I. V., Bersenev, Yu. S., Ganin, A. A., Barner, K., Schunemann, J. W., and Heinemann, K., "Pressure derivative of T_c in amorphous $(Fe_{100-x}Mn_x)_{75}P_{15}C_{10}$ alloys", J. Magn. Magn. Mater., 124(3), 293-297, 1993 .

[12] Kraus, E., Heinemann, K., Barner, K., Khan, F. A., Medvedeva, I. V., Schicketanz, H., and Terzieff, "Thermoelectric power of some $(Fe_{1-x}Mn_x)_{75}P_{15}C_{10}$ amorphous alloys", Phys. Stal. Sol. (a), 177, 547-553, 2000.

[13] Sinha, A. K., "Magnetic transition from an amorphous ferromagnetic $Fe_{75}P_{15}C_{10}$ to an amorphous antiferromagnetic $Mn_{75}P_{15}C_{10}$", J. Appl. Phys., 42, 338-342, 1971.

[14] Hasegawa, R., "Magnetic properties of an amorphous Mn-P-C alloy", Phys. Rev. B3, 1631-1634, 1971.

[15] Yao, Y. D., Yen, T. Y., Jen, S. U., "Transport properties of amorphous and crystalline $(FeV)_{80}B_{14}Si_6$", Chinese J. Phys., 26(4), 207-211, 1988.

[16] Sovak, P., Pavlik, G., Kolesar, V., Saksl, K., Fuzer, J., "Structure and magnetic properties of $Fe_{73.5-x}V_xCu_1Nb_3Si_{13.5}B_9$ alloys", Rev. Adv. Mater. Sci., 18, 518-521, 2008.

[17] Roys, S. B., Nigam, A. K., Chandra, G., and Majumder, A. K., "Electrical resitivity and magnetoresistance in Fe-B-C amorphous alloys", J. Phys. F: Met. Phys., 18, 2625-2633, 1988.

[18] Tsuei, C. C., and Lilienthal, H., "Magnetization distribution in an amorphous ferromagnet", Phy. Rev. B, 13, 4899-4906, 1976.

CHAPTER 2
THEORETICAL PERSPECTIVE

2.1 Classification of amorphous alloys

The amorphous alloys classify into five groups to facilitate the discussion of the electron transport properties of these non-periodic substances. The Bloch theorem fails in a non-periodic system and, hence, the mean free path of sp conduction electrons is certainly shorter than that in a crystal. Thus, the d electrons at the Fermi level having more localized character can contribute to the electron conduction, together with sp electrons.

The behavior of the conduction electrons becomes more complex in magnetic systems because of their interaction with magnetic moments. The classifications of the amorphous alloys are discussed below.

Group (I): Ferromagnetic, having T_c well above of 300K. The carrier of the fermi level is mainly d electrons. (i. e. alloys Fe–Co–Zr, Fe–Co–B–Si, Co–B)
Group (II): Weakly ferromagnetic, having T_c well below of 300 K. The carrier of the fermi level is mainly d electrons. (i. e. alloys Fe–Zr, Fe–Hf)
Group (III): It has no spontaneous magnetization over the whole temperature range. But they exhibit a strongly temperature dependent magnetic susceptibility. Those exhibiting spin-glass behaviors and the Kondo effect are included in this group.
The carrier of the fermi level is mainly d electrons or (d+sp) electrons. (i.e. alloys Fe–Mn–B–Si, Pd–Si–Mn)
Group (IV): It is non-magnetic, with a fairly large Pauli paramagnetism. The carrier of the fermi level is mainly d electrons or (d+sp) electrons. (i. e. alloys Cu–Zr, Cu-Ti, Ni-Zr, Y-Al, La-Al, Ca-Al, Ca-Mg, Ni-P)
Group (V): It is also non-magnetic, with a small Pauli paramagnetism. The carrier of the fermi level is mainly d electrons or sp electrons. (i. e. alloys Mg–Zn–Ga, Ag–Cu–Mg, Ag–Cu–Ge, Mg–Cu)

2.2 Electron transport properties of liquid and amorphous metals

One of the most challenging objectives in the studies of liquid and amorphous alloys is to gain a deeper insight into the electron conduction mechanism in non-periodic systems. Electron conduction in amorphous alloys is certainly due to electrons at fermi surface, whose number density generally amounts to the order of $10^{22}/cm^3$. However, a breakthrough was brought about by the Ziman theory put forward in 1961, which successfully explained the electrical resistivity behavior of simple liquid metals like pure Na and Zn [1]. This implies that the Ziman theory had been widely accepted as a valid model for liquid metals in group (V). But the role of d electrons in group (IV) still remained unsettled at that time. Unfortunately, however, the measured resistivity and its temperature dependence had been frequently discussed on the basis of the Ziman theory for simple liquid metals without seriously considering the limit of its applicability. To avoid complications due to possible d electron contributions, we choose the nearly-free-electron model where the resistivity decreases slightly with increasing temperature in the amorphous phase. Thus, the temperature coefficient of resistivity, TCR ($=(1/\rho)(d\rho/dT)$) is negative in the amorphous phase. Crystallization proceeds in two steps at about 400 K and 500 K for this group and is accompanied by a larger drop in resistivity at the second crystallization. The TCR becomes positive after complete crystallization. It is clear that not only the magnitude of the resistivity is substantially different but also the sign of TCR changes between amorphous and crystalline phases. In contrast, the resistivity in the liquid phase is close to the value obtained by extrapolating the temperature dependence of the resistivity in the amorphous phase, and its TCR is negative in agreement with that in the amorphous phase. Characteristic features of the electrical resistivities of liquid and amorphous alloys are summarized below.

1. The residual resistivity of amorphous alloys is generally in the range 20-1000 μΩ-cm and is 5-100 times that in the crystallized phase. The resistivity values in amorphous alloys are comparable to liquid metals.
2. The resistivity of amorphous alloys changes with temperature only by a few % over the temperature range 2-300K. The change in resistivity with temperature is also fairly small in liquid metals.

3. The sign of TCR in amorphous alloys and liquid metals is either positive or negative and is sometimes extremely close to zero, depending on the composition of a given alloy system.

Thus the electron transport properties of amorphous alloys are definitely different from those in crystals but are seemingly similar to those of the corresponding liquid phase. However, there exists a distinctive difference in the electron transport mechanism between liquid and amorphous phases.
Elastic scattering dominates in the liquid phase whereas inelastic scattering and/or the quantum interference effect play a key role in the amorphous phase at temperatures below 300K.

2.3 Electron transport theories in a disordered system

The negative TCR phenomenon is a characteristic feature of a semiconductor with a well-defined energy gap. Thus, one may address a naive question as to why a negative TCR, though its magnitude is small, appears for many liquid and amorphous alloys, in which the carrier concentration is as high as $10^{22}/cm^3$ and a well-defined fermi edge exists without any energy gap. Various theories have been proposed to shed more light on the electron transport mechanism including the origin of a negative TCR in a disordered metallic system. The Ziman theory developed for simple liquid metals was frequently employed without much success to explain the occurrence of a negative TCR observed in various amorphous alloys in groups (I) to (IV). Apart from the Ziman theory, the Anderson localization theory [2] has played a crucial role in the progress of the electron theory of a disordered system. N, F. Mott [3, 4] has made further important contributions to this field and laid the basis for the concept of the weak localization effect.

2.4 Important characteristics of the electrical resistivity of metallic glasses

Two important characteristics of the electrical resistivity of metallic glass are:
(1) Their resistivity is relatively high, greater than 100 μΩ-cm at room temperature.
(2) Their TCR is very small and can be positive or negative.

The combination of these two properties leads to a very high residual resistivity at 0 K. The high resistivity of amorphous alloy compared with that of the same alloy in the crystalline state is related to the increased scattering of the conduction electrons due to a random atomic arrangement. In such a random structure, the phonon contribution to the scattering of electrons is small, hence the small TCR. A single theory which not to be able to provide any quantitative description of the low temperature transport properties of the transition metal alloy. Moreover, there are no theoretical grounds for believing that there is common explanation for the anomalous behavior of the resistivity with respect to temperature because of complicated interplay between configuration, thermal and magnetic disorder [5]**.**

2.5 Ziman theory for simple liquid metals

Ziman resistivity formula is constructed on the basis of the following three assumptions.

(i) Firstly, the linearized Boltzmann transport equation is assumed. It implies that the mean free path of the conduction electron must be longer than an average atomic distance and, hence, the Ziman theory will work only for systems with resistivities less than about 150 μΩ-cm.

(ii) Secondly, the Born approximation is assumed to calculate the transition probability. This is justified by the pseudopotential approach, which holds only for systems in group (V) but fails for systems in group (IV).

(iii) Thirdly, elastic scattering is assumed.

This limits the applicability of the Ziman formula only to liquid metals, because elastic scattering dominates either at very low temperatures or at temperatures well above the Θ_D. The sign of TCR can also be predicted from Ziman theory. When the temperature of a liquid metal is increased, an increase of free volume and structural disorder is obtained. The resistivity will increase with increasing temperature for monovalent metals. This explains well the occurrence of a positive TCR in monovalent and polyvalent metals. The Ziman theory also explains the negative TCR for divalent metals with increasing the temperature that contributes to reduce the resistivity.

2.6 Baym–Meisel–Cote theory for amorphous alloys

Among the three underlying assumptions in the Ziman theory, the linearized Boltzmann transport equation and the Born approximation are equally justified for amorphous alloys. However, the assumption of the elastic scattering collapses in amorphous alloys, since their electron transport properties are discussed at temperatures well below the Θ_D or below 300K in most cases. At such low temperatures, ions can no longer be treated as independent particles but the concept of collective excitations of phonons must be introduced to treat the thermal vibrations of ions. A proper evaluation of the inelastic electron-phonon interaction is of prime importance in dealing with the electron transport properties of amorphous alloys at temperatures below Θ_D. The Ziman theory has abandoned and, instead, employs the Baym resistivity formula as a starting equation through which the inelastic electron–phonon interaction is incorporated. The details have been described by Meisel and Cote [6, 7]. The temperature dependence of the resistivity for amorphous alloys is well approximated as

$$\rho = \left[\rho_0 + \Delta\rho(T)\right] \exp[-2W(T)] \tag{2.1}$$

$$W(T) = W(0)\left(\frac{T}{\Theta_D}\right) + \ldots \tag{2.2}$$

Where, ρ_0 is the residual resistivity at 0 K, $\Delta\rho(T)$ is the term arising from the inelastic electron-phonon interaction and the exponential term $\exp[-2W(T)]$ represents the Debye–Wallar factor. The term $\Delta\rho(T)$ is shown to exhibit $+T^2$ dependence at lower temperatures and +T at higher temperatures. The Debye-Wallar factor yields $(1-\alpha T^2)$ dependence at lower temperature and the $(1-\beta T)$ at higher temperatures. The quantity α and β are the TCR's at lower and higher temperature respectively. The validity of equation (2.1) has been experimentally confirmed [8, 9] for amorphous alloys. In the case of amorphous alloys with resistivities at room temperature lower than about 50–60 μΩ-cm, the term $\Delta\rho(T)$ dominates and $+T^2$ dependence is observed at temperatures below about 90K whereas +T at temperatures above about 90K. Hence, the TCR is positive over the whole temperature range 2–300K. This ρ–T behavior is hereafter called type (a) and is illustrated in figure 2.1.

As ρ gradually increases beyond 60 μΩ-cm, the Debye–Waller factor begins to play a more important role at higher temperatures. Type (b) is assigned to the ρ–T behavior characterized by $+T^2$ dependence at lower temperatures but (1-βT) at higher temperatures. This naturally results in a shallow resistivity maximum at an intermediate temperature, as shown in figure 2.1. With increasing ρ, the resistivity maximum is shifted to lower temperatures and finally vanishes [8, 9]. Now the ρ–T dependence is dominated only by the Debye–Waller factor over the whole temperature range: $(1-\alpha T^2)$ at lower temperatures and (1-βT) at higher temperatures. This is type (c), which is obviously characterized by a negative TCR over the whole temperature range. Type (c) is generally observed amorphous alloys with resistivities in the range 100–160 μΩ-cm.

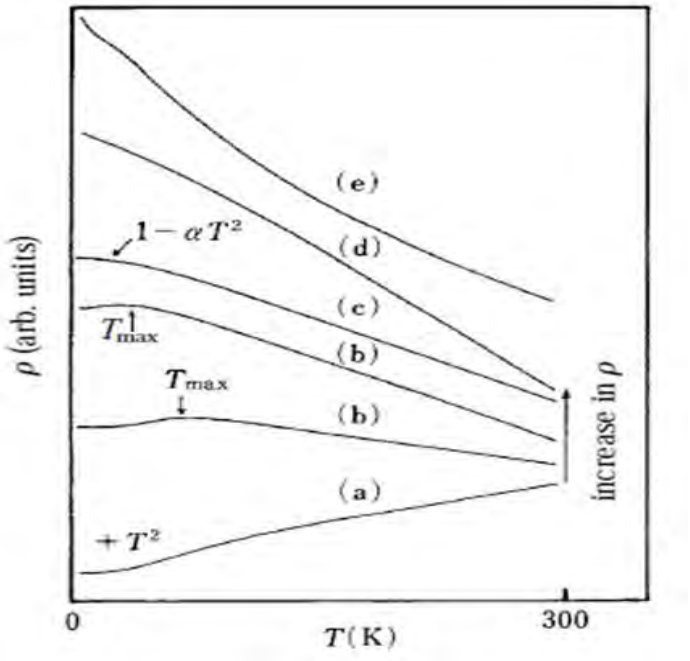

Figure 2.1.Temperature dependent of resistivity of amorphous alloys

They always appear in the sequence (a) → (b) →(c) → (d) → (e) with increasing resistivities, as illustrated in figure 2.1. The gradual change in types (a) → (b) → (c) is accompanied by shortening of the mean free path down to an average atomic distance [8, 9]. An increase in resistivity in this regime is due entirely to the mean free path effect and is free from the band structure effect.

Indeed, the data are well explained in terms of equation (2.1) within the framework of the Baym–Meisel–Cote theory based on the Boltzmann transport equation. The sign of TCR shown in figure refers to that near room temperature and, hence, a positive TCR corresponds to type (a) whereas a negative TCR to the remaining types (b) → (e). This means that the sign of TCR in amorphous alloys is determined by the interplay between $\Delta\rho(T)\exp[-2W(T)]$ and $\rho_0\exp[-2W(T)]$ in equation (2.1). The ρ–T behavior of types (d) and (e) are exclusively observed in high-resistivity amorphous alloys with resistivities exceeding about 200 μΩ-cm. This indicates that the mean free path is shortened to an average atomic distance of a few Å. An increase in resistivity in this regime should be caused by a change in the electronic structure, since the mean free path can no longer be decreased.

2.7 Anderson localization theory

According to the Anderson localization theory the conduction electron with an average energy E_0 are loosely bound in the periodic potential. The Bloch wave derived from the tight-binding approximation will form a relatively narrow band with a width W. Now some disorder is introduced into the potential distribution. Its amplitude is assumed to vary irregularly in the range $-V_0/2<V<+V_0/2$. Anderson [4] proved that all electrons within the band cannot form the Bloch wave but localize in real space, if the ratio V_0/W exceeds some critical value. At finite temperatures, localized electrons will be able to exchange their energy with phonons and to hop from one site to another. This is termed hopping conduction. The Anderson localization theory has been further elucidated by Mott and others and concepts such as weak localization, mobility edge, and minimum metallic conductivity, scaling law and metal–insulator transition have been established. The inelastic electron–phonon interaction plays a key role in determining the temperature dependence of the electrical resistivity in amorphous alloys but its contribution becomes less important as the residual resistivity increases. The residual resistivity arises from the elastic scattering of conduction electrons due to random distributions of ions at absolute zero. The elastic scattering is indeed essential in the Anderson localization theory.

2.8 Mooij correlation for metallic glasses

Mooij [10] pointed out a remarkable correlation between the magnitude of electrical resistivity in concentrated disordered transition metallic alloys and its TCR. He observed that a large number of disordered alloys containing transition metals have similar conduction properties, both in bulk and as a thin film. These anomalous conduction properties are probably caused by the very small electron mean free path in these materials. Furthermore, Mooij observed that TCR changes sign in a relatively narrow range of resistivity (i. e., the critical resistivity for which TCR=0, $\rho_c \approx$ 100-160 μΩ-cm). In the literature, a resistivity value of 160 μΩ-cm has often been given fundamental significance in the sense that it serves as a universal boundary which divides the positive TCR and negative TCR's. For ρ>160 μΩ-cm, the resistivity usually decreases as temperature T increases, in contrast to the normal metallic behavior seen for lower resistivity systems. Most theoretical approaches to the Mooij correlation are based on quantum-mechanical coherence effects, namely, the incipient Anderson localization. It has been argued that the breakdown of the adiabatic approximation, leads to phonon-assisted tunneling and, therefore, to a negative TCR. To explain these results it can be noted that the high resistivity of all these materials indicates that the conduction electron mean free path is small. A rough estimate for NiCr, based on the Boltzmann transport [11] and assuming one conduction electron per atom yields a mean free path of 4 Å, only slightly larger than the interatomic distance. The high scatter in these materials is usually caused by the high amount of disorder. This disorder can be the random distribution of the elements over the lattice sites in a disordered alloy; in other materials it is also the structural disorder of an amorphous solid. In the compounds with a low TCR the strong scatter is probably of magnetic origin [12]. In alloys containing transition metals the scatter is increased by the possibility of s-d scatter [11]. The behavior of electrical conduction in the alloys with a low TCR can be understood to a great deal if it is assumed that in these alloys a lower limit is reached in the electron mean free path. Such a limit must exist, as the mean free path cannot be smaller than the interatomic distance [13]. If this limit is reached, a further decrease of the mean free path due to phonons is impossible and a low TCR results. Between different alloys the interatomic distance and the conduction electron density only vary within rather narrow limits, and this explains why all resistivities lie in a restricted range.

In the same way the insensitivity of the electrical properties to changes in crystal structure and the limited and gradual effect of additions of other elements can be understood. However, a negative TCR is frequently observed. A straightforward explanation within this model is only possible if it is assumed that the number of conduction electrons increases with temperature. It may be that localization of electrons due to the high scatter leads to the occurrence of bound states, from which the electrons can be thermally excited. It is of course also possible that the occurrence of a negative TCR is due to some completely different mechanism. In all cases the correlation between TCR and the resistivity suggests that the negative contribution to TCR becomes larger as the resistivity increases. This phenomenon is found in disordered metallic systems, especially in concentrated disordered alloys. Nearly always these systems contain at least one transition metal. The origin of this phenomenon is probably associated with the strong scatter in these materials. Many, but not all, properties of these materials can be explained on the basis of the assumption that the electron mean free path in these systems is near to a lower limit.

2.9 Ziman-Faber theory for metallic glasses

Disordered and glassy metals are a challenge to understand since they require theories that differ markedly from those employed to describe crystalline and liquid states of matter. Several of the anomalous physical properties of disordered metals have resisted clear explanations for over a decade. In particular, these materials often exhibit negative TCR that are difficult to reconcile with any of the existing transport theories. The Ziman-Faber theory of resistivity in highly disordered metals yields quantitative results. In this theory the resistive structure factor and the x-ray structure factor are assumed to be identical; the temperature dependence of this structure factor determines the temperature dependence of the resistivity. However, in disordered solids the x-ray and resistive structure factors are significantly different [14].

2.10 Differential thermal analysis (DTA)

DTA is the process of accurately measuring the difference of temperature in between the test sample and the reference when both are being heated or cooled at the same rate under identical environment.

Differences in temperature between the test sample and reference may arise when physical or chemical changes take place in the test material. The change of temperatures are observed either by endothermic or exothermic peak as a function of time or temperature. These changes may due to dehydration, transition from one crystalline variety to another, destruction of crystalline lattice, oxidation, hydrogenation, melting and boiling of the materials etc. Hence reference is used as a baseline which is thermally stable and uncreative i.e. no reaction can take place with the reference sample. Metallic glasses, which are in a metastable state, can crystallize when heated or held at elevated temperatures for a sufficient time. Crystallization involves a change in properties, such as heat capacity, electrical resistivity, volume and magnetization properties [15]. DTA techniques are the most frequently used method to study the crystallization behavior. However, the reaction needs to occur with a relatively large heat of crystallization and is not very useful when the reaction rate is slow or if only a small heat transfer is involved. The crystallization behavior of metallic glasses has been extensively studied [16-21]. An amorphous phase is metastable and does not exist in the equilibrium phase diagram. Hence, it crystallizes upon heating. The temperature at which crystallization occurs is referred to as the T_x and is generally several degrees higher than the T_g. Figure 2.2 illustrates the temperature dependence of the free volume of a given substance.

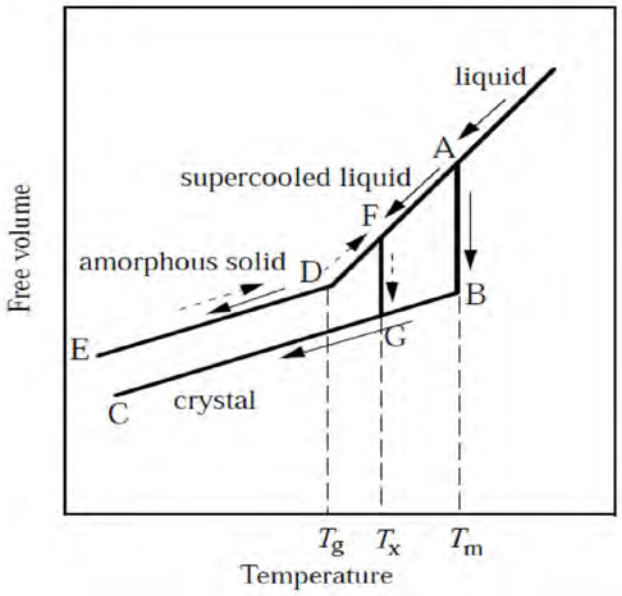

Figure 2.2. Temperature dependent of free volume of amorphous alloys

The volume of a liquid decreases with decreasing temperature and discontinuously drops upon solidification at the T_m, as can be seen in figure 2.2 (line AB). During the cooling process, the supercooling phenomenon may occur. This is apt to proceed, particularly if the cooling rate is very high. The motion of atoms in a supercooled liquid becomes sluggish as the supercooling proceeds. If its viscosity exceeds some critical value of about 10^{13} poise, the motion of the atoms is practically frozen. This result gives the formation of an amorphous phase. The temperature at which the viscosity reaches this critical value is called the T_g. Upon heating, the amorphous phase may enter the supercooled liquid state, if crystallization is somehow suppressed across the T_g, but eventually crystallizes, say, at a temperature at point F below the T_m. The volume corresponding to the first derivative of the free energy is continuous but its slope changes across the T_g marked as the point D. The same is true in the temperature dependence of the entropy. Thus, the specific heat corresponding to the second derivative of the free energy shows a discontinuous jump at T_g. Both the T_x and T_g can be experimentally determined using DTA or DSC. In DTA measurement, an amorphous alloy is heated together with a reference material possessing approximately the same heat capacity as the sample. DTA records the temperature difference between them as a function of temperature. The relation $T_g<T_x<T_m$ generally holds. We can determine both T_g and T_x from the measured spectra, since a small endothermic reaction occurs at T_g but the exthothermic reaction occurs at T_x in the heating process. It is to be noted that they are not properties inherent in a given amorphous alloy but depend on the heating rate. It may also be noted that the DTA measurement allows us to determine the enthalpy difference between an amorphous phase and the crystallized phases by integrating the total area of the exothermic peak upon crystallization.

2.10.1 The endothermic reaction

Reactions are accompanied by the absorption of heat is known as endothermic process or reactions. Reactions of this type require a continuous supply of energy from the outside to keep them going. For example, the reaction of hydrogen and iodine to form hydro-iodic acid takes place with absorption of heat.

The compounds which are formed by endothermic reactions, such hydrogen peroxide, H_2O_2 and hydro-iodic acid, HI, are thermally unstable. This means that the internal energies of the molecules of H_2O_2 and HI tend to break the bonds holding the atoms together.

e.g. $H_2 + I_2 = 2HI$ 1.2 kcal.

$C + 2S = CS_2$ 1.5 kcal.

2.10.2 The exothermic reaction

The reactions which are accompanied by the evolution of heat, is known as the exothermic reaction. Exothermic reaction may proceed in the absence of any supply of energy from outside. The burning of magnesium, carbon, methane, etc, in air, are all exothermic reactions.

e.g. $C + O_2 = CO_2 + 97$ kcal

$2Mg + O_2 = 2MgO + 148$ kcal

Thus, carbon will continue to burn in oxygen with the evolution of heat until the supply of carbon or oxygen is exhausted. It may be noted here that compounds which are formed by highly exothermic reactions, such as carbon dioxide, magnesium oxide, are stable towards heat. These are said to be thermally stable. This means that a very high temperature is required to separate them into their component elements.

2.10.3 Peak area, peak temperature

When no reaction occurs in the specimen, no temperature difference between the specimen and the reference sample is observed. But as soon as a reaction commences the specimen becomes hotter or cooler than the inert material and thus a peak develops on the curve for temperature difference against time ($\Delta T/t$) or temperature ($\Delta T/T$). Along the line AB the difference is zero since no reaction is occurring but at B an endothermic reaction starts and gives rise to the peak BCD with its minimum at C, where, the rate of heat absorption by the reaction is equal to the difference between the rate of supply of heat to the specimen and to the inert material.

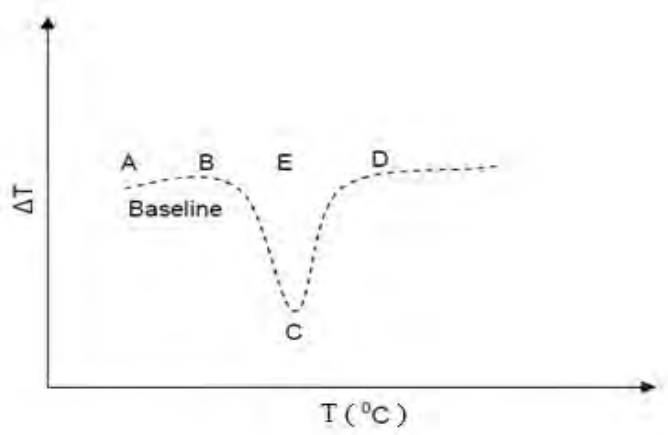

Figure 2.3. Variation of DTA curve with temperature

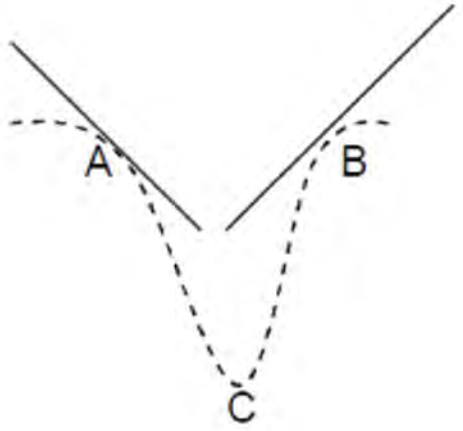

Figure 2.4. DTA endothermic peak analysis of the sample

Peak area (BC × DE) is proportional to the amount of reacting material. The distance BD is usually referred as the peak width and the distance EC as the peak height or amplitude. The area enclosed by the peak has to be accurately determined for quantitative work. In this method two tangents are drawn on both sides of the peak and a straight line AB joined the points of tangency. The area enclosed by ABC formed the peak area. Peak area increases with rapid change of temperature (i.e. rate of heating). Peak shape change with finer particle size to more reaction centers.

The random stacking of the layers, coupled with disruption caused by removal of inter layer water, would be expected to expose more nuclei to dehydration at any moment for a given weight of mineral as slow heating rate reduces the sharpness of the peaks unduly and very fast rates tend to cause overlapping of neighboring reactions.

2.10.4 Activation energy

The minimum amount of energy that must be provided by a collision for reaction to occur is called the activation energy, E_{act}.

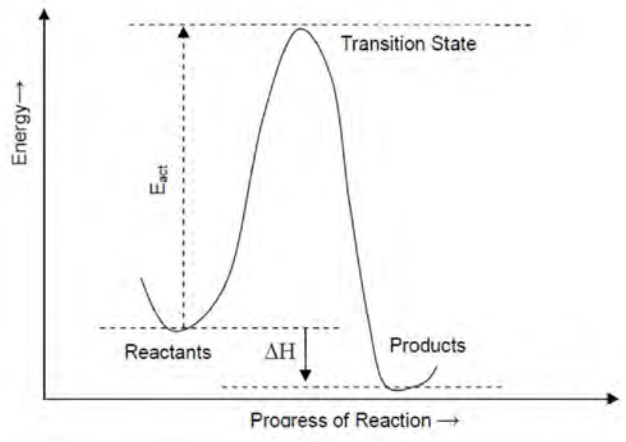

Figure 2.5. Activation energy for a reaction to start in DTA experiment

When heat is liberated, the heat content enthalpy H of the molecules themselves must decrease the change in heat content. ΔH is therefore given a negative sign. In the case of an endothermic reaction, where heat is absorbed, the increase in heat content of the molecules is indicated by a positive ΔH. ΔH is the difference in energy content between reactants and products, so E_{act} is the difference in energy content between reactant and transition state.

2.10.5 Change of phase

A change of phase or phase change occurs when a crystalline solid becomes liquid or when a liquid becomes a vapor, or when the reverse of either of these processes takes place.

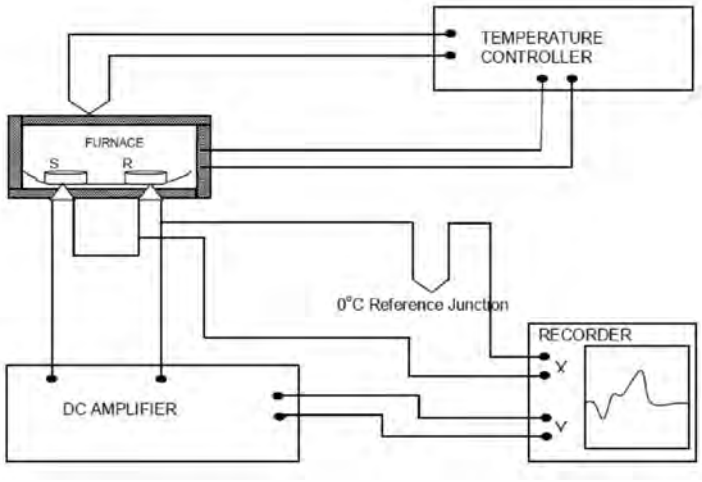

Figure 2.6. A schematic diagram of the DTA assembly

DTA assembly consists of the following parts:

(i) A sample holder to place the sample.

(ii) Thermocouples for measuring temperatures.

(iii) A furnace to heat the sample.

(iv) A program controller to heat the sample at a uniform rate.

(v) A recorder for registering the temperature difference between the sample and the reference material.

2.11 Thermo gravimetric (TG)

TG has been done at the same time of the experiment of DTA to compare the result of DTA. The TG means the mass loss or mass gain at different temperatures often calculated at percentages. The TG results are usually shown in graphical mood in which the temperature or time is plotted against mass change in percentage. When any reaction occurs, the reaction may be endothermic or exothermic may also associated with mass change due to evaporation of fundamental element from the sample or may be the mass gain due to new formation of compound.

2.12 Differential thermo gravimetric (DTG)

DTG calculates the rate of mass change at any temperature with respect to the differential change of temperature or time at that temperature. This calculation is done in association with a TG analysis. It is done for the following reason. Some time in TG curve, there may be one peak due to two or more successive reactions that happens with in a very short time interval and that cannot be detected with the TG peak. TG gives one peak for very close successive reactions. On the other hand, the DTG peaks are so useful tool that it can differentiate very clearly that closed reactions with giving separate peaks for each of the successive reactions. In DTG analysis the dm/dT is plotted against temperature or time. At the peak the rate of mass loss or gain is maximum. The area under the DTG peak is proportional to the mass change *dm*. Height of the peak at any time or temperature indicates the rate of mass change at that temperature

2.13 Magnetoresistance (MR)

The MR refers to the change in electrical resistance of a specimen in response to the magnetic field applied to the specimen externally. The resistance change occurs with the magnetic field when the field is sufficient enough to change the orientation of the electrons of the atoms. In that case the path of the electron becomes curved and do not go exactly in the direction of the superimposed electric field. The change of orientation of the atomic electrons occurs such that the conduction electron find more mean free path with less number of collision with the atomic ions and the atomic electrons, then the resistance decreases other wise it increases or remain constant.

When the resistance of a material changes with the application of the magnetic field, the material is said to have the MR. The MR usually expressed in percentage and is calculated by the following way.

$$MR\% = \frac{R(H) - R(0)}{R(0)} \times 100\% \qquad (2.3)$$

Where, R (H) is the resistance in presence of magnetic field and R (0) is the resistance in absence of magnetic field.

All metals show some MR, but upto only a few percent. Nonmagnetic metals such as Au, exhibits small MR, but the magnitude is somewhat greater (upto 15%) in ferromagnetic metals such as Fe and Co. The semimetal Bi also shows~18% MR in a transverse field of 0.6T which rises to a 40 fold change at 24T [22]. Cu is more typical in the same very powerful field (24T) gives rise to change of only ~ 2% at room temperature. This is the classical positive magnetoresistance that varies as B^2 (B=applied magnetic field) in metallic ferromagnet such as CrO_2, Fe_3O_4 at low temperature [23]. It is absent in the free electron gas [24] but appears when the fermi surface is non spherical. This MR originates from the impact of the Lorentz force on the moving charge carriers similar to the Hall effect. Its value is ~10% at 10T. The phenomenology of the MR effect is similar to that of magnetostriction. This effect can be classified into two categories:

(i) One is the part, which depends on the intensity of spontaneous magnetization that corresponds to the volume magnetostriction.
(ii) The second is that change caused by the rotation of spontaneous magnetization, which corresponds to the usual magnetostriction.

Mott interpreted this phenomenon in terms of the scattering probability of the conduction electrons into 3d holes. If the substance is in a ferromagnetic state, half of the 3d shell is filled up, so that the scattering of 4s electrons into the plus state of 3d shell is forbidden. This scattering is however, permitted in a nonmagnetic state in which both the plus spin state and the minus spin state of the upper 3d levels are vacant. Mott explained the temperature variation of resistivity fairly well by this model. Kasuya interpreted this phenomenon from a standpoint quite different from Mott theory. He considered that d electrons are localized at the lattice points and interact with the conduction electrons through the exchange interaction. At 0^0K the potential for the conduction electron is periodic, because the spin of 3d electrons of the entire lattice points in the same direction. At finite temperature, spins of 3d electrons are thermally agitated and the thermal motion may break the periodicity of the potential. The 4s electrons are scattered by an irregularity of the periodic potential which results in additional resistivity.

Kasuya postulated that the temperature dependence of the resistivity of ferromagnetic metal is composed of a monotonically increasing part due to lattice vibration and an anomalous part due to magnetic scattering, the magnitude of the later being explained by this theory. The effect of high temperature has been treated in two different approaches. The first approach [25] is to consider a constant exchange interaction between magnetic atoms and a random distribution of the local anisotropy field is considered which changes with temperature. The other approach is to consider a distribution of exchange integral in order to take into account the fluctuation in the amorphous alloys [26]. Both the approaches are unrealistic and in fact no rigorous theory of the high temperature behavior for amorphous material has been developed.

2.14 Hall effect

The ordinary Hall effect was discovered in 1879 by Edwin Hall. It refers to the difference in potential produced on the opposite sides of a conductor when a current is flowing in the presence of a magnetic filed applied perpendicular to the current. The effect arises from the Lorentz force acting on a moving charge in a magnetic field that curves its trajectory away from its straight-line path. This causes charge to accumulate on one side of a conductor and create a potential difference across the opposite sides of a conductor. Other origins for the Hall effect which included the asymmetric scattering (known as skew scattering) from impurities with spin-orbit coupling. There are indeed two different manifestations of spin-orbit scattering contributing to the additional Hall effects (called the extraordinary Hall effect). The first is skew scattering and the second is the side jump [27] which arises not only from spin-orbit scattering of impurities, but also from ordinary scattering when the electron conduction wave functions have their spin and orbit coupled together.

The Hall effect in magnetic materials is measured using the geometrical configuration as shown in figure 2.7. If the magnetic field is applied along the z direction and the electrical current is applied along the x-direction of a specimen, the resulting Hall voltage generated along the y-direction. A conduction electron subject to the Lorentz force contributes to the Hall effect.

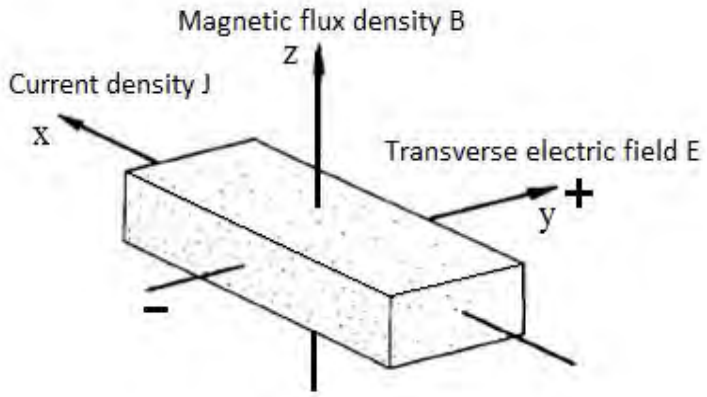

Figure 2.7. The geometry for the Hall effect measurement

If the Hall resistivity ρ_H is defined as the ratio of the transverse electric field E_y over the current density J_x, we have the relation $\rho_H=R_HB_z$ for non-magnetic materials. Obviously, measured values of ρ_H, when plotted against the applied magnetic induction B_z, fall on a straight line passing through the origin, since R_H is independent of B_z. This is, however, no longer true in magnetic metals because of the additional contribution arising from the localized magnetic moment. Figure 2.8 shows the Hall resistivity of the ferromagnetic alloy as a function of the magnetic field applied along the z-direction.

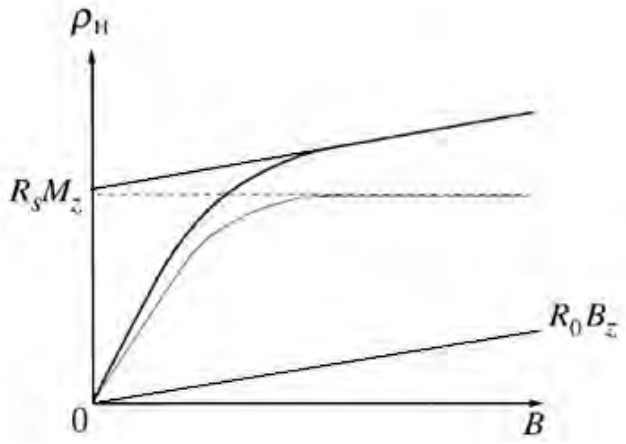

Figure 2.8. The Hall resistivity is decomposed into the normal and anomalous contributions

It is seen that the Hall resistivity initially increases very rapidly but its slope becomes small with increasing magnetic field. The non-linear behavior of the ρ_H–B curve is decomposed into the normal Hall effect due to the Lorentz force and a strongly temperature dependent component proportional to magnetization M_z, and is explicitly written as

$$\rho_H = E_y/J_x = R_0 B_z + R_s M_z \qquad (2.4)$$

Where R_0 is the normal Hall coefficient and R_s is the anomalous Hall coefficient. The second term can be present in a ferromagnetic domain even in the absence of an applied field. Thus, it is a spontaneous contribution to ρ_H in this case. The anomalous Hall coefficient is deduced from a slope of the ρ_H–B curve at high magnetic fields while the normal Hall coefficient can be roughly estimated from the initial slope. The details about the Hall coefficient in ferromagnetic metals will be found in the literature [28].

2.15 Principle of vibrating sample magnetometer (VSM)

The VSM has become a widely used instrument for determining magnetic properties of a large variety of materials: diamagnetic, paramagnetic, ferromagnetic and antiferromagnetic. The method was developed by S. Forner [29] and on the flux change in a coil when the sample is vibrated near it. It has a flexible design and combines high sensitivity with easy of sample mounting and exchange. Samples may be interchange rapidly even at any operating temperature. Measurement of magnetic moment is small as 5×10^{-5} emu/g is possible in magnetic fields from zero to 4T. Maximum applied fields of 2T are reached using conventional laboratory electromagnets. VSM normally operate over a temperature range of 20 to 1050 K. When the sample of a magnetic material is placed in a uniform magnetic field, a dipole moment proportional to the product of the sample susceptibility times the applied field is induced in the sample. If the sample is made to undergo a sinusoidal motion, electrical signal is induced in suitability located stationary pick-up coils. This signal which is at the vibrating frequency, is proportional to the magnetic moment, vibration amplitude and vibration frequency.

In order to obtain the reading of the moment only, a capacitor is made to generate another signal for comparison which varies in its moment, vibration amplitudes and vibration frequency in the same manner as does the signal from the pick up coil. These two signals are applied to the inputs of a differential amplifier, and because the differential amplifier passes only difference between the two signals, the effect of vibration amplitude and frequency changes is cancelled. Thus only the moment determines the amplitude of the signal at the output of the differential amplifier. This signal is in turn applied to a lock-in amplifier, where it is compared with the reference signal which is at its internal oscillator frequency and is also applied to the transducer which oscillates the sample rod. Thus the output of the lock-in amplifier is proportional to the magnetic moment of the samples only avoiding any noise of frequency other that of the magnetic moment of the signal. The absolute accuracy of this system is yields an accuracy of 0.05% of full scale. The absolute accuracy of this system is better than 2% and reproducibility is better than 1%. Least measurable moment is 5×10^{-4}emu. Variation magnetic field is achieved with a Newport Electromagnet Type 177 with 17.7 cm diameter pole pieces. The magnet is mounted on a graduated rotating base. The standard model is modified to provide an adjustable pole gap in order that the highest possible field strength is available. The field can vary from 0 to 1 T and is measured directly by using Gauss meter.

2.15.1 Electronic circuits of the VSM

The functions of the associated electronic circuits are

(i) to permit accurate calibration of the signal out put from the detection coils.

(ii) to produce a convenient AC output signal which is directly related to the input and which can be recorded

(iii) to produce sufficient amplification for high sensitivity operation.

The block diagram of an electronic circuit used for the VSM consists of a mechanical vibrator, a sine wave generator, an audio amplifier, a ratio transformer, a phase-shifter, a lock-in amplifier, 4 pick-up coils system, a reference coil system, an electric power supply, an electromagnets and PID regulator as shown in figure 2.9. The sample magnetized by the electromagnet generates an e.m.f. in the pick up coils PC. The strength of this signal is proportional to the magnetization of the sample.

The vibrating permanent magnet also generates an e.m.f. of fixed amplitude in the surrounding reference coils. This reference signal is stepped down with the help of a ratio transformer so that its amplitude is equal to that sample signal. The two signals are then brought in phase and put to the lock in amplifier. The lock in amplifier works as a null detector. Limits of sensitivity are determined by signal to noise ratio at the input circuit, where noise is defined as any signal not arising from the magnetic moment of the sample. The major sources of noise are the Johnson noise of the wire used for the pick up coils and the magnetic responses of the sample holder, which superimposes undesired signals in phase with the wanted signal.

Use of a minimum mass of weakly diamagnetic materials for a sample holder, carefully checked to contain no ferromagnetic impurities, is essentials to minimize this coherent noise contribution.

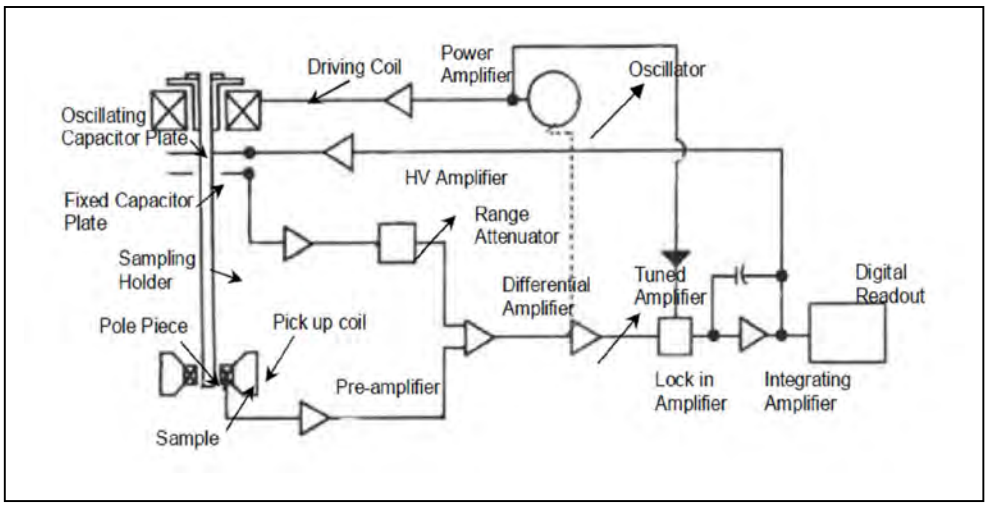

Figure 2.9. Electronic circuits of the vibrating sample magnetometer (VSM)

Corrections for the small magnetic contribution of the samples holder can then be made by measurements with the sample removed. This correction is much less than the equivalent case with a moving coil system. We used a standard sample for the calibration which was spherical shaped specimens of mass 152mg of pure nickel (99.99%). With only the lock-in amplifier and the oscilloscope as a null detector, it was found that 152mg nickel sample signal could be balanced reproducibility. Such reproducibility indicated that the long time drifts caused by the combined effects of vibration, amplitude changes and frequency changes a bridge sample position and offer effects were negligible.

The pick-to-pick vibration amplitude has been varied from 0.1mm to 1.0 mm in order to examine errors caused by amplitude changes. Frequencies of 100Hz or less permit the use of inexpensive components and minimize eddy current shielding by the vacuum chamber. The measurements are completely independent of eddy currents in the surrounding parts, if the measurements and calibration are made at the same temperature. Mechanical coupling between the vibrating system and the fixed detection coils must be avoided. Although the coils are arranged for minimum sensitivity to external vibration, a noticeable background signal is obtained when the vacuum chamber contacts the detection coils. Such mechanical effects are difficult to eliminate electronically, because the spurious background signal has the same frequency as the sample signal and maintains a constants phase differences with respect to the sample signal. Usually the magnetometer and detection coils are both supported by the magnetic coupling, so that some mechanical coupling may be noticed as highest sensitivity.

References

[1] Ziman, J. M., “Electrons and phonons: the theory of transport phenomena in solids”, Oxford university press, 1960.

[2] Anderson, P. W., Phys. Rev., “Absence of diffusion in certain random lattices". Phys. Rev.”, 109, 1492-1505, 1958.

[3] Mott, N. F., “The minimum metallic conductivity in three dimensions”, Phil. Mag., B44, 265-284, 1981.

[4] Mott, N. F., “Metal–insulator transitions”, Taylor & Francis Ltd, 1990.

[5] Brouers, F., and Brauwers, M., “On the temperature dependence of electrical resistivity in concentrated disorder transition binary alloys”, J. Phys. Paris, 36, L-17, 1975.

[6] Meisel, L. V., and Cote, P. J., “Electrical resistivity in low resistivity amorphous alloys”, J. Non Cryst. Sol., 61 & 62, 1307-1312, 1984.

[7] Meisel, L. V., and Cote, P. J., “Critical test of the diffraction model in amorphous and disordered metals”, Phys. Rev., B17, 4652-1459, 1978.

[8] Mizutani, U., “The magnetism of amorphous metals and alloys”, Prog. Mat. Sci., 28, 97-228, 1983.

[9] Mizutani, U., “Electron transport in non-periodic metallic systems: amorphous alloys and quasicrystals”, Phys. Stat. Sol. (b), 176, 9-30, 1993.

[10] Mooij, J. H., “Electrical conduction in concentrated disordered transition metal alloys”, Phys. Stat. Sol. (a), 17, 521-530, 1973.

[11] Ziman, J. M., “Electrons and Phonons”, Clarendon Press, Oxford, 1960.

[12] Buschow, K. H. J., and Van Daal, H. J., “Proc. cof. Magnetism and Magnetic Materials Chicago”, 1971, Ed. Graham, C. D., J_R. and Rhyne, J. J., Amer. Inst. Phys., New York, 1972.

[13] Mott, N. F., and Davies, E. A., “Electronic processes in non-crystalline materials”, Clarendon press, Oxford, 1971.

[14] Fritsch, G., Dyckhoff, W., Pollich, W., Zottman, W., and Luscher, E., “The thermo power of amorphous CuTi alloys as a function of concentration and temperature”, Z. Phys. B, 59, 27-34, 1985.

[15] Scott, M. G., “Amorphous Metallic Alloys, Ed. Luborsky, F. E., Butterworths, London, p.144, 1983.

[16] Greer, A. L., “Crystallization Kinetics of $Fe_{80}B_{20}$ Glass”, Acta Metallurgica, 30(1), 171-192, 1982.

[17] Morris, D. G., “Crystallization of the metglas-2826 amorphous alloy”, Acta Metallurgica, 29(7), 1213-1220, 1981.

[18] Gao, Y., Zhang, S., Liu, B., "Crystallization behavior of melt–spun $Nd_7Fe_{86}Nb_1B_6$ ribbons under different heating rates ", J. Magn. Magn. Mater., 208, 158-162, 2000.

[19] Pratap, A., Raval, K.G., Gupta, A., Kulkarni, S. K., “Nucleation and growth of a multicomponent metallic glass”, Bull. Mater. Sci., 23(3), 185-188, 2000.

[20] Botta, W. J., Negri, D., Yavari, A. R., “Crystallization of Fe-based amorphous alloys”, J. Non Cryst. Sol., 247, 19-25, 1999.

[21] Takahara, Y., “Irreversible structural relaxation in Fe–B–Si amorphous alloys”, Mater. Sci. Eng. A, 231, 128-133, 1997.

[22] Pippard, A. B., “Magnetoresistance”, Cambridge University Press, Cambridge, UK, 1984.

[23] Watts, S. M., Wirth, S., Von Molnar, S., Barry, F., and Coey, J. M. D., “Evidence for two-band magneto transport in half-metallic chromium oxide”, Phys Rev B, 61, 149621, 2000.

[24] Ashcroft, N., and Mermin, B., “Solid state physics”, Holt Richart and Winstone New York, 1976.

[25] Harris, R., Phischke, M., and Zucherman, M., “New model for amorphous magnetism”, J. Phys. Rev. Lett., 31, 160-162, 1973.

[26] Polak, C., Knobel, M., Grossinger, R., Sato Turtell, R., “The development of nanocrystalline $Fe_{13.5}Nb_3Si_{13.5}B_9$ magnetism and structural disorder”, J. Magn. Magn. Mater., 134, 1-12, 1994.

[27] Berger, L., and Bergmann, G., “The Hall effect and its applications”, Eds. Chien, C. L., and Westgate, C. R., Plenum, New York, p.55, 1979.

[28] Hurd, C. M., “The Hall effect in metals and alloys”, Plenum Press, New York, 1972.

[29] Forner, S., “Versatile and sensitive vibrating sample magnetometer”, Rev. Sci. Instr., 30, 548-557, 1959.

CHAPTER 3

PREPARATION OF AMORPHOUS MATERIALS

3.1 Introduction

For a long time, it was believed that amorphous system could not exist in ferromagnetism. It was abolished by the discovery of metallic glass by J. W. Klement et al in 1960 [1]. The argument was based on the evidence that the electronic band structure of crystalline solids did not changes in any fundamental way on transition on the liquid state. A real technological interest developed after the preparation of continuous ribbons of amorphous alloys [2]. The theoretically expected retention of ferromagnetic behavior in amorphous solids was first demonstrated by Marder and Nowick in their work on vacuum deposited Co-Au alloys and soon thereafter [3] their work on split-cooled Pd-20at% Si containing some ferromagnetic element.

3.2 Preparation technique of amorphous ribbon

In terms of viscosity and diffusion co-efficient we can find the conditions for formation of glass. In metals viscosity is low but the diffusion co-efficient and mobility is high. In the case of amorphous material viscosity is very high but the mobility and the diffusion co-efficient is low. Atomic bonds tend to be covalent as in the case of silicate (SiO_2). There are various techniques used to produce a metallic alloy in an amorphous state. The different experimental techniques developed to produce amorphous metallic glass can be classified into two groups. The atomic deposition method and the fast cooling melt method.

3.2.1 The atomic deposition methods

The atomic deposition methods include condensation of a vapor on a cooled substrate by vapor deposition, sputtering deposition, electro deposition and chemical deposition. Deposition can be described in terms of whether the added atom is prevented from diffusing more than an atomic distance before it is fixed in position.

3.2.2 The fast cooling of the melt

For producing of an amorphous state by any of the liquid quenching devices, the alloy must be cooled very fast from T_m to T_g. The factors controlling T_g and T_x are both structural and kinetic. The structural factors are concerned with atomic arrangement, bonding and atomic size effects. The kinetic factors as discussed by Turnbull [6] are the nucleation, crystal growth rate and diffusion rate compared to the cooling rate. The interest in this method stems from the wide variety of alloys that can be made as well as from the potential low cost of preparation. In the pioneering work [7], a number of devices have been reported for obtaining the necessary high quenching rates and for producing continuous filaments. The methods using the principle of fast cooling of melt techniques are:

(i) The gun technique (ii) The melt spinning technique (iii) Double roller rapid quenching technique (iv) Centrifuge and rotary split quenching technique (v) Torsion catapult technique (vi) Plasma-jet spray technique (vii) Filamentary casting technique (viii) Melt extraction technique (ix) Free jet spinning technique

Although the different methods are used in preparing amorphous metallic ribbons, only the melt spinning technique was used to prepare the metallic ribbons for the present work.

3.2.2.1 The melt spinning technique

Melt spinning technique [8] was used to prepare the $(Fe_{100-x}V_x)_{75}P_{15}C_{10}$ (x=0, 5, 10 and 15) metallic glasses in the form of ribbon. In order to prepare the samples, the required quantities of metal-metal or metal-metalloid alloys are taken in a quartz tube in their stoichiometric ratio wt%. A set of heater coils are surrounded the quartz tube and this coil is connected to the rf power generator. The temperature of the heater coil is kept more than the melting temperature of the alloy compound. The melt is kept above the melting point of alloy until a homogeneous mixing in obtained. An inert gas flows through the quartz tube after the homogeneous mixing is formed. Then the molten alloys fall on a rotating copper wheel through the outlet of the quartz tube. This alloy is cooled at an ultra-fast rate with the help of the rotating copper wheel.

On impact with the rotation drum, the melt is frozen within a few milli-second and producing a long ribbon of metallic glasses. The experimental set up used for the above process is shown in figure 3.1. The metallic glass ribbons are usually prepared in a furnace with an argon atmosphere (0.2 to 0.3 atmps). The buttons prepared are of about 50 grams each. Care is taken to ensure thorough mixing and homogeneity of the alloy composition, by turning over and re-melting each button few times. The mother alloys, formed in the form of buttons in a furnace by sudden cooling, are then cut into small pieces and is inserted in the quartz tube. The quartz tube is connected to the argon cylinder through a valve and a pressure gauge. After proper cleaning of the roller surface and adjusting its speed to the desired value, as measured by stroboscope, the induction furnace is powered using high frequency rf power generator.

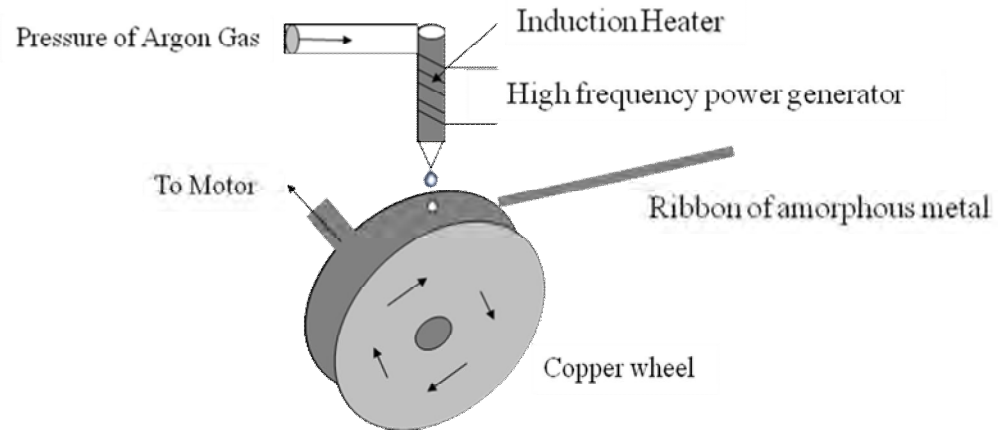

Figure 3.1. Experimental set up used for the melt spinning technique

When the melting temperature is reached as observed through a protective spectacle, the injection pressure is applied by opening the pressure valve. To avoid the turbulence of the wind, arising from the high speed roller in distributing the melt puddle, cotton pad and metallic shield are usually used just beneath the roller. To avoid oxidation of the ribbon during its formation, an inert atmosphere is created around the roller by a slow stream of helium gas. The speed of the roller, the volumetric flow rate, the orifice diameter, the substrate orifice distance, the injection angle etc. are adjusted by trial and error to get the best result in respect of the quality and the geometry of the ribbons. Important factors to control the thickness of ribbons are as follows.

(i) Angular velocity, $\omega \sim 6000$ rev/min or surface velocity, $v \sim 25$ m/s.

(ii) Gap between the nozzle and rotating copper drum is ~ 100 to 150 μm.

(iii) Oscillations of the rotating copper drum both static and dynamic have maximum displacement of ~ 1.5 μm

(iv) Pressure from 0.2 to 0.3 argon atmosphere.

(v) Temperature of the metal $T_m \approx 1500\ ^{\circ}C$. The temperature should not exceed 1800° C otherwise quartz tube would melt.

(vi) Stability is ensured for the drop to fall on the surface of the spinning drum.

References

[1] Klement, J. W., Willens**,** R. H., and Duwez, P., "Non-crystalline structure in solidified gold-silicon alloys", Nature, 187, 869-670, 1960.

[2] Pond, R. Jr., and Maddin, R., "The solubility of carbon in cobalt and nickel", Trans. Met. Soc. ALME, 245, 2475-2476, 1969.

[3] Tsuei, C. C., and Duwez, P., "Metastable amorphous ferromagnetic phases in palladium base alloys", J. Appl. Phys., 37, 435, 1966.

[4] U. Mizutani, "The magnetism of amorphous metals and alloys", Prog. Mat. Sci., 28, 97-228, 1983.

[5] U. Mizutani, "Electron transport in non-periodic metallic systems: amorphous alloys and quasicrystals", Phys. Stat. Sol. (b), 176, 9-30, 1993.

[6] Turnbull, D., "Bulk metallic glass matrix composites", Contemp. Phys., 10, 473-488, 1969.

[7] Duwez, P., Willens, R. H., and Klement, Jr. W**.,** "Amorphous Metallic Alloys", J. Appl. Phys., 31, 1136-1137, 1960.

[8] Budhani, R. C., Goel, T. C., and Chopra, K. L., "Melt spinning technique for preparation of metallic glasses", Bull. Mater. Sci., 4(5), 549-561, 1982.

Chapter 4

EXPERIMENTAL TECHNIQUES

4.1 XRD measurement

Bragg reflection is a coherent elastic scattering in which the energy of the X-ray is not changed on reflection. If a beam of monochromatic radiation of wavelength λ is incident on a periodic crystal plane at an angle θ and is diffracted at the same angle as shown in Fig. 3.1, the Bragg diffraction condition for X-rays is given by

$$2d\sin\theta = n\lambda \qquad (4.1)$$

Where, d is the distance between crystal planes and n is the positive integer which represents the order of reflection. Equation (4.1) is known as Bragg law. It suggest that the diffraction is only possible when $\lambda \leq 2d$ [1].

For this reason we cannot use the visible light to determine the crystal structure of a material. X-ray diffraction (XRD) provides substantial information on the crystal structure.

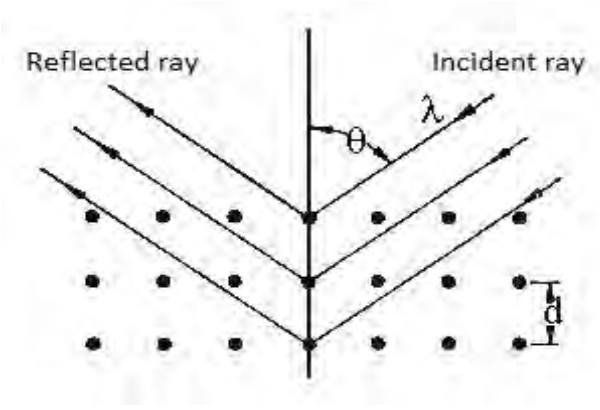

Figure 4.1. Bragg law of XRD

An X'Pert PRO XRD PW 3040 (Phillips) XRD was used to get X-ray data for the samples at the Magnetic Materials Division of the Atomic Energy Centre of Dhaka.

The powder diffraction technique was used with a primary beam power of 40 kV and 30 mA for Cu radiation. A nickel filter was used to reduce CuKα radiation and finally CuKα radiation of wave length λ=1.54178 Å was used for the XRD measurement.. The 2θ values were carried out from 30° to 65°. The sampling pitch and the time for each stem data collection were 0.02° and 1.0 s respectively. All data of the samples were stored in a computer memory and later analyzed them using computer software "X'PERT HIGHSCORE". XRD was carried out with an X-ray diffractometer for the powder samples of $(Fe_{100-x}V_x)_{75}P_{15}C_{10}$ (x=0, 5, 10 and 15).

4.2 Lattice parameter determination

In the present case, the lattice parameter (a) of the BCC structure was calculated for (110) plane of the annealing temperature of 400 °C and 450 °C for 30 minutes annealing time by the following equation [1].

$$a = d_{hkl}\sqrt{h^2 + k^2 + l^2} \tag{4.2}$$

The lattice parameters (a and c) of the hexagonal structure were calculated for the planes (116) and (214) of the annealing temperature from 500 °C to 650 °C for 30 minutes annealing time by the following equation [1].

$$\frac{1}{d_{hkl}^{\ 2}} = \frac{4(h^2 + hk + k^2)}{3a^2} + \frac{l^2}{c^2} \tag{4.3}$$

where, $d_{hkl} = \dfrac{\lambda}{2\sin\theta}$ and λ=1.54178 Å for CuKα radiation.

h, k and l are the indices of the crystalline plane.

4.3 Grain size determination

The crystalline grain size of the powder samples was estimated from the broadening of the corresponding X-ray spectral peaks using the Scherrer formula [2].

$$L = \frac{0.9 \times \lambda}{(B - 0.05) \times \cos\theta} \tag{4.4}$$

Where L is the grain size, λ the wavelength of the CuKα radiation (λ=1.54178 Å), 0.05 is the instrumentation broadening, B is the full width at half-maximum (FWHM) of a diffraction peak expressed in radians and θ is the Bragg angle.

4.4 DTA, TG and DTG measurements

The transition temperature of the samples was monitored by a differential thermal analyzer [Seiko-Ex-STAR-6300, Japan]. The measurements of DTA, TG and DTG were carried out from 40 °C to 600 °C at a heating rate of 20 °C min^{-1} under nitrogen gas flow. The DTA traces give the crystallization temperature as determined from the exothermic versus temperature curves where as the TG curves provides the percentage of weight change with respect to temperature. DTG curves give the small change of mass with a small difference heating temperature. For this purpose we used the lab facility of Bangladesh Council of Scientific and Industrial Research (BCSIR), Dhaka.

4.5 Surface morphology measurement

Hitachi S-3400N variable pressure SEM was used for surface morphology of the as prepared samples as shown in figure 4.2. For this purpose we used the lab facility of Bangladesh Council of Scientific and Industrial Research (BCSIR), Dhaka.

Figure 4.2. External view of Hitachi S-3400N scanning electron microscope

SEM measurement setup

(i) Accelerating voltage=15000V, (ii) Deceleration voltage=0V,

(iii) Magnification=100, (iv) Working distance=9800 um, (v) Emission current=70000 nA, (vi) Photo size=1000, (vii) Micron marker=500000,

(viii) Sub magnification=0, (ix) Specimen bias=0 V, (x) Condencer1=50000,

(xi) Scan Speed= Slow3, (xii) Calibration scan speed=8, (xiii) Color mode=Grayscale, (xiv) Condition=Vacuum=15kV (xv) Magnification= x100, (xvi) WD=9.8mm

(xvii) Stage position X=47880000, Y=28511000, Z=10000000.

4.6 Resistivity measurement by four probe technique

There are various types of techniques for resistivity measurements. Here, we have used four-point probe technique for the measurement of resistivity. In this technique, two of the probes were used to measure the potential difference between two points, while the other terminals were used to pass current through the sample as shown in figure 4.3. The resistance is then calculated from the slope of current versus voltage curve after fitting the trend (straight) line. To avoid the difficulty, silver glue were used for the electrical contacts.

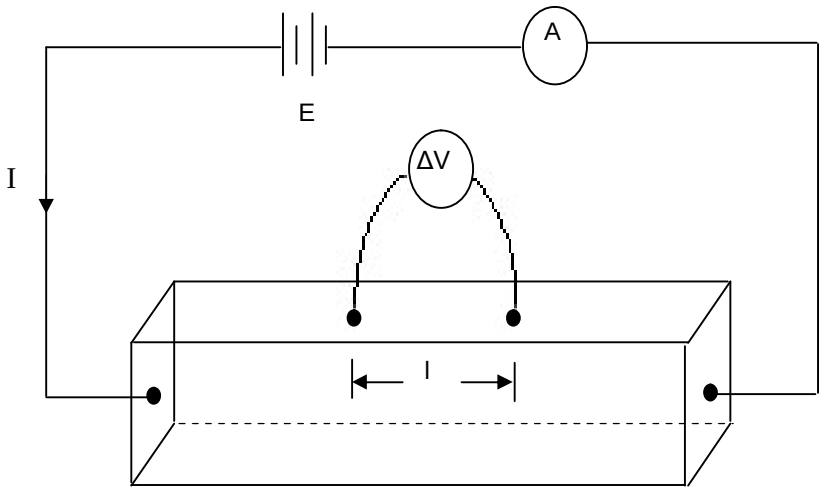

Figure 4.3. Four probe technique to measure the resistivity

The resistivity of the samples was calculated by using the following formula [3].

$$\rho = R \times \frac{A}{l} \tag{4.5}$$

Where, R is the resistance of the sample, A is the cross-sectional area which is the product of the width and thickness and the length between inner probes is l. However, to measure the resistivity as a function of temperature and Hall resistivity at room temperature, this four-probe technique has been used with the above experimental setup. Current (0 mA to 200 mA with an interval of 10 mA) was passed through the sample from the regulated power supply in constant current mode (Model 6177C) and the corresponding voltage across the inner two probes were recorded by Keithley digital nanovoltmeter (Model 181).

4.6.1 Temperature dependent of resistivity measurement

The experimental setup of the temperature dependence of resistivity of the rectangular strip size samples were measured at low temperature (298 K- 93 K) in a liquid nitrogen atmosphere as shown in figure 4.4.

Figure 4.4. Low temperature resistivity measurement setup

In this set up both the sample and the thermocouple were attached in the sample holder and lowered slowly in the liquid nitrogen atmosphere. Hewlett-Packard constant-current power supply (Model 6177C) and Keithley digital nanovoltmeter (Model 181) along with chromel constantan thermocouple were used in the measurement setup.

At this position (0 mA to 200 mA with an interval of 10 mA) current passed through the sample from the regulated power supply and the corresponding voltage across the inner two probes has been recorded by the digital voltmeter. The measurements were taken from 298 to 93K with an interval of 10 K.

4.7 Magnetoresistance (MR) measurement at room temperature

When the resistance of a material changes with the application of the magnetic field, the material is said to have the MR. The measurement of MR was done by the calculation method of resistivity. It was also measured by the standard four-probe technique as discussed in section 4.6. The MR of the samples was calculated by using the following formula [4].

$$MR(\%) = \frac{\rho(H) - \rho(H=0)}{\rho(H=0)} \times 100 \qquad (4.6)$$

Where, ρ(H=0) is the resistivity at zero magnetic field and ρ(H) is the resistivity at any magnetic field (H=0-0.57 T).

4.8 Hall resistivity measurement at room temperature

The Hall-coefficient is related to the electric field in the y-direction (E_y), the electric current density in the x-direction (J_x) and the component of the magnetic field in the z-direction (H_z) by the following relation.

$$R_H = \frac{E_y}{J_x B_z} \qquad (4.7)$$

Consider a specimen with the geometry as shown in figure 4.5. Three quantities must be measured for this measurement. Magnetic field along the z direction (H_z), voltage developed along the y direction (V_y) and current along the x direction (I). The current density can be determined by dividing the total current by the cross-sectional area of the sample. Thus $H_z=H$, $J_x=I/wt$ and $E_y=V_y/t$

$$R_H = \frac{wV_y}{IH} \qquad (4.8)$$

Where, t is the thickness and w is the width of the sample.

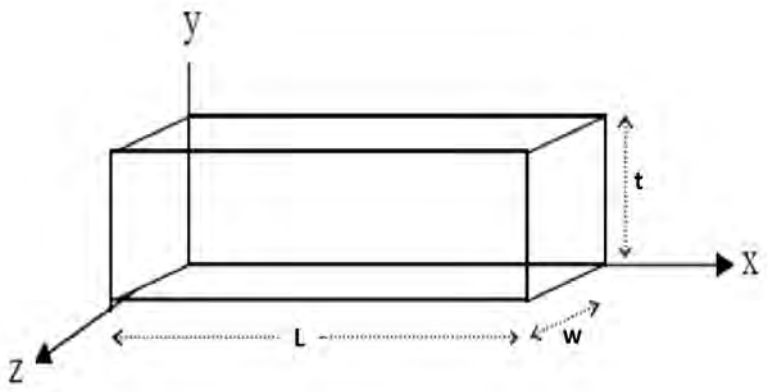

Figure 4.5. Hall resistivity measurement

Thus the Hall resistivity is measured bythe following formula [4].

$$\rho_H = R_H A/L \qquad (4.9)$$

Where, A is the area of the cross section and L is the length.

4.9 Magnetization measurement at room temperature

Magnetization is the magnetic moment per unit volume. There are various ways of the measuring of magnetization. A high quality, low cost vibrating sample magnetometer (VSM) for the study of magnetic properties of materials in high magnetic fields in the temperature range 80-350 K has been constructed by A. Niazi et al [5]. In the present work, DC magnetization was measured by using a home built VSM at room temperature with magnetic field from 0 to 1.172 kG as shown in figure 4.6. The sample, usually a sphere or small disc, was cemented to the lower end of a rod while the other end was fixed to a mechanical vibrator. Current through the vibrator with a frequency of about 37 Hz and peak to peak amplitude of about 7 V in a direction at right angles to the magnetic field. The oscillating magnetic field of the sample induces an alternation emf in the direction coils. The vibrating rod also carries a reference specimen, in the form of a small permanent magnet near its upper end; the oscillating field induces another emf in two reference coils. The two voltage form two sets of coils are compared, and the difference is proportional to the magnetic moment of the sample.

Figure 4.6. Vibrating sample magnetometer (VSM) setup

4.9.1 Calibration of the VSM

We calibrated the VSM using a 152 mg spherical sample of 99.99% pure nickel. The sample was made spherical with the help of the sample shaping device. The saturation magnetic moment of the sample has been calculated using available data. The ratio transformer reading was obtained by the following relation.

$$M=KK^{/} \qquad (4.10)$$

Where M is magnetic moment, $K^{/}$ is saturation ratio transformer reading and K is VSM calibration constant.

But

$$M=m\sigma \qquad (4.11)$$

Where, σ is the specific magnetization and m is the mass of the sample.
From (4.7) and (4.8) the calibration constant is given by

$$K=m\sigma/K^{/} \qquad (4.12)$$

The accuracy of this calibration, however, depends on the reliability of the standard nickel sample, the accuracy of the ratio transformer and the gain of amplifier. The equipment was operated repeatedly with the same standard sample and stability was found to be within 1 part in 100. The absolute accuracy of the instrument depends on the knowledge of the magnetic properties of the calibration standard and reproducibility of the sample position. When the substitution of calibration was used, the major error ± 1% was introduced by the estimation of standard nickel sample.

The relative accuracy of these instruments depends on accurate calibration of the precision resistor divider network. The total error here can be kept less than 0.5%. A typical calibration curve of VSM is shown in figure 4.7.

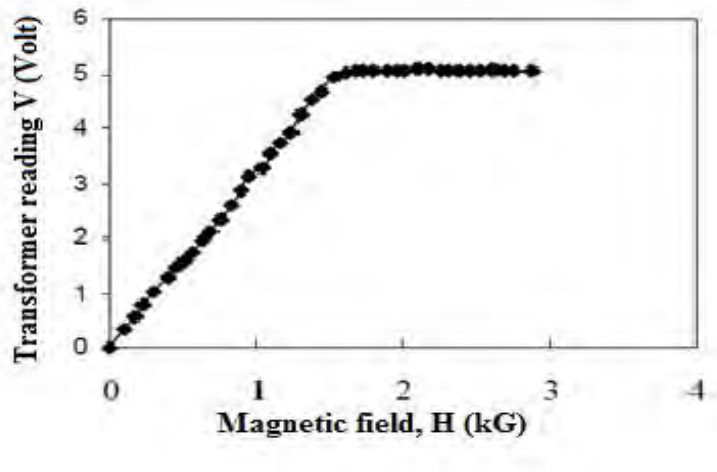

Figure 4.7. Calibration curve of VSM

Calibration data

(i) Sensitivity =100μV (ii) Reference phase =89.9° (iii) Time constant =1 sec (iv) Peak to peak voltage =7V (v) Bandwidth =12dB (vi) Reference frequency f=37Hz (vii) Mass of the pure nickel m =152×10^{-6} kg (viii) Bohr magneton of pure nickel s =58.5 Am^2/kg (ix)) Ratio transformer reading $K^{/}$ =5.05V (x) Saturation magnetic field= 1.8 kG.

Putting the of m, $K^{/}$ and s values in equation (4.9) we get

$K= 152\times10^{-6}\times58.5/5.05$

$= 1.76$ emu/V

The magnetization of the ribbons samples were calculated by using the following equation [4].

$$M = \frac{KV}{m} \tag{4.13}$$

Where, M= Magnetization of the experimental sample, m= Mass of the experimental sample, V= Voltage correspond to the magnetization, K= Calibration constant of the VSM

The relation between the saturation magnetization (M_s) and the Bohr magneton (μ_B) per formula of $(Fe_{100-x}V_x)_{75}P_{15}C_{10}$ (x=0, 5, 10 and 15) are as follows [6].

$$\mu_B = \frac{M}{5585} \times Ms \tag{4.14}$$

Where, M is the molecular weight of the substance.

References

[1] Kittel, C., "Introduction to solid state physics", 7th edition, John Wiley & Sons, Inc., Singapore, 1996.

[2] Klue, H. P., Alexander, L. E., "X-ray diffraction procedures for polycrystalline and amorphous materials", John Wiley & Sons, New York, p. 627, 1997.

[3] Halliday, D., Resnic, R., Walker, J., "Fundamentals of physics", 6th edition, John Wiley & Sons, Inc., p. 611, 2001.

[4] Cullity, B. D., "Introduction to magnetic materials" Addition-Wisley publishing company, Inc., California, 1972.

[5] Niazi, A., Poddar, P., Rastogi, A. K., "A precision, low cost vibrating sample magnetometer (VSM)", Current science, 79, 99-109, 2000.

[6] Smit, J., "Magnetic properties of material", McGraw-Hill, New York, 1971.

CHAPTER 5

RESULTS AND DISCUSSION

5.1 XRD analysis for as prepared samples

Since the width of the as prepared ribbons was very small (~ 0.8 mm), it was not possible to measure the XRD from this ribbon samples. For this reason, some ribbons (no. 10-15) of the as prepared samples of the same composition were taken into a crucible and were ground carefully until it became fine powder. XRD data was taken of this fine powder to check the amorphous nature. The 2θ values were carried out from 30° to 65° by using an X'Pert PRO XRD PW 3040 (Phillips) and CuKα radiation (λ=1.54178 Å). Figures (5.1-5.4) shows the XRD pattern of the as prepared $(Fe_{100-x}V_x)_{75}P_{15}C_{10}$ (x=0, 5, 10 and 15) samples in powder form.

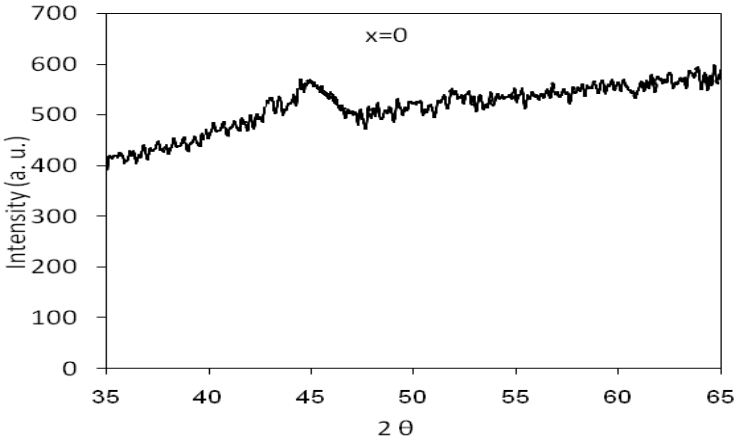

Figure 5.1. XRD of the as prepared $Fe_{75}P_{15}C_{10}$ sample in powder form

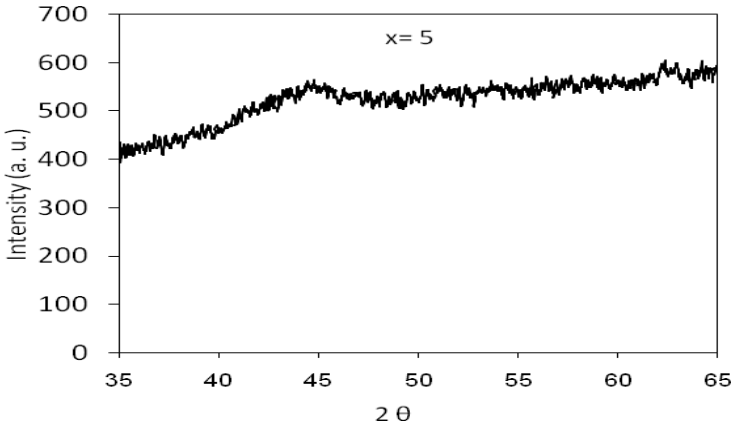

Figure 5.2. XRD of the as prepared $Fe_{71.25}V_{3.75}P_{15}C_{10}$ sample in powder form

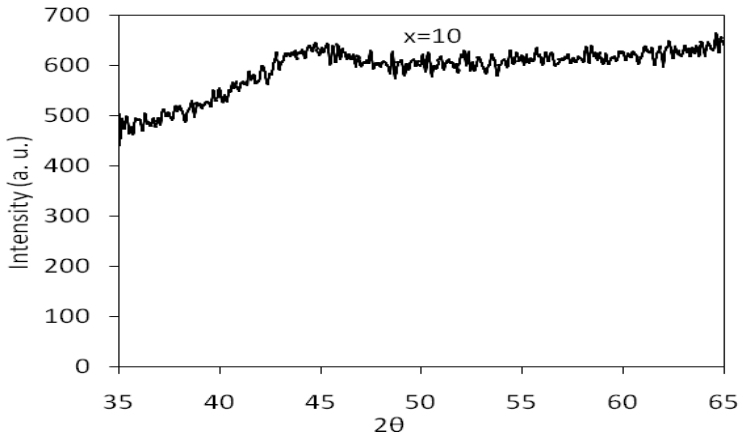

Figure 5.3. XRD of the as prepared $Fe_{67.5}V_{7.5}P_{15}C_{10}$ sample in powder form

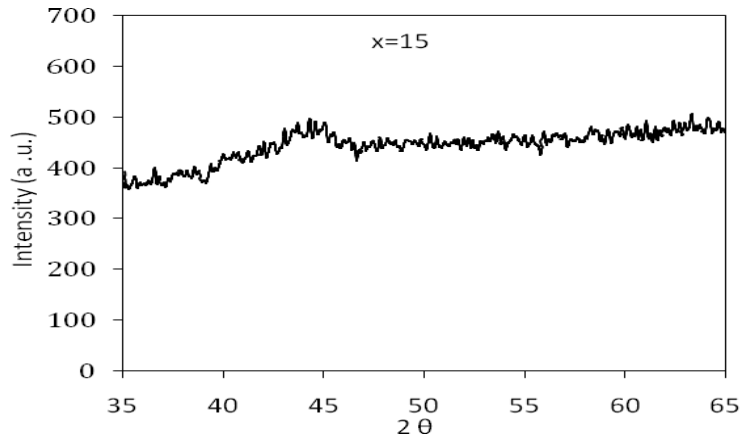

Figure 5.4. XRD of the as prepared $Fe_{63.75}V_{11.25}P_{15}C_{10}$ sample in powder form

We have seen that each figure of the as prepared samples contains a broad peak within the 2θ values from 42° to 47° which confirms the samples are amorphous in nature.

5.2 XRD analysis for re-crystallization phenomenon

To show the re-crystallization phenomenon of this alloy, the fine powder was put in an aluminum foil (1.5 cm×1.5 cm) and folded it. The folded sample was put in a digital furnace (Carbolite, Sheffield, England) at annealing temperature 400 °C for 30 minutes annealing time. Then the furnace was switched off and allowed to cool to room temperature. When the furnace had cooled down to room temperature, the sample was taken out and ground until it became fine powder.

Then the XRD was taken of this fine powder. The power samples were annealed at 400 °C, 450 °C, 500 °C, 550 °C, 600 °C and 650 °C for 30 minutes annealing temperature and XRD data were taken in each case. The whole procedure was repeated for the other composition. Figures (5.5-5.8) shows the XRD pattern of the $(Fe_{100-x}V_x)_{75}P_{15}C_{10}$ (x=0, 5, 10 and 15) alloys of annealing temperature from 400 °C to 650 °C for 30 minutes annealing time . The diffraction peaks were identified as (301), (231), (112), (110) and (411) planes at around 35°, 40°, 43°, 45° and 46° for Fe_3P, Fe_3P, Fe_3P, αFe and Fe_3P respectively. Vanadium phosphides are not expected to show clearly as the larger V content is only 11.25% of the Fe content. The pattern of the samples for temperatures between 400 °C and 450 °C are consistent with a BCC structure.

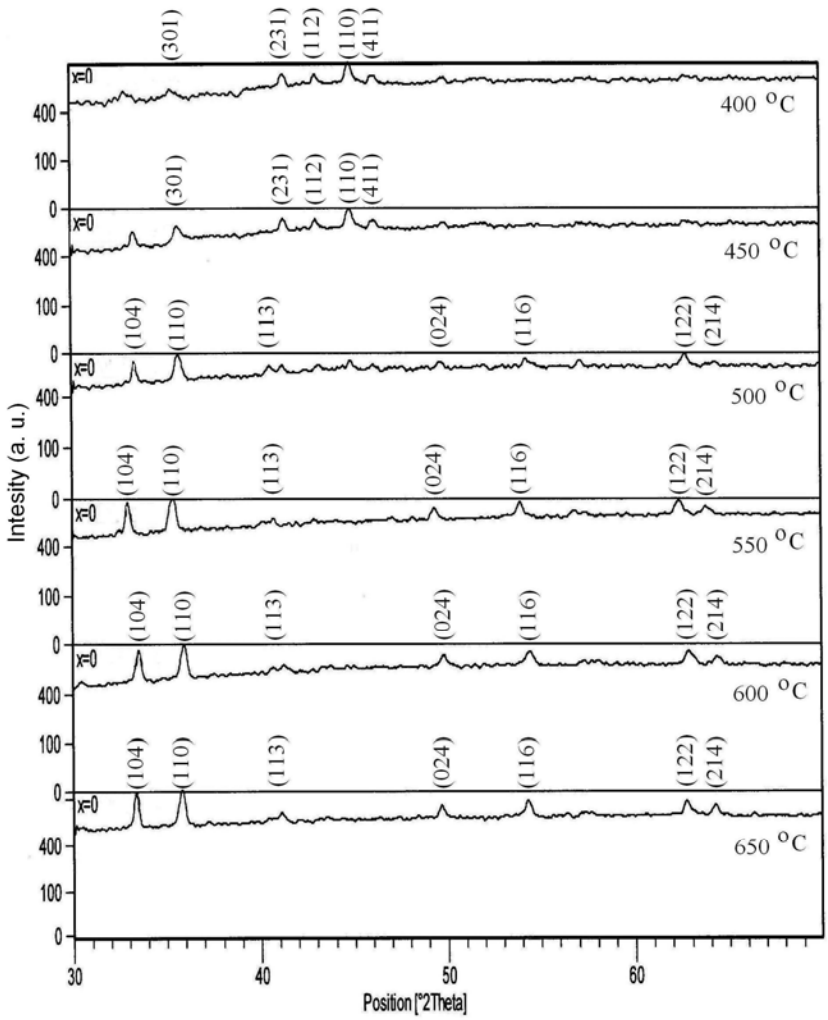

Figure 5.5. XRD for $Fe_{75}P_{15}C_{10}$ powder sample at annealing temperatures from 400 °C to 650 °C for 30 minutes annealing time

The lattice parameter (a) of the BCC structure was calculated by using the following formula [1].

$$a = d_{hkl}\sqrt{h^2 + k^2 + l^2} \qquad (5.1)$$

Where, h, k and l are the indices of the crystalline plane.

At 400 °C the lattice parameter 'a' of the samples for (110) plane is 2.854 Å, 2.859 Å, 2.864 Å and 2.869 Å and at 450 °C it is 2.852 Å, 2.854 Å, 2.857 Å and 2.857 Å for x=0, 5, 10 and 15 respectively. The lattice parameter increases with increasing of V content into the samples. The increase in lattice parameter and hence the unit cell volume with increasing V content is due to a volume expansion effect as V has the larger atomic radius (1.92 Å) compared to Fe (1.72 Å).

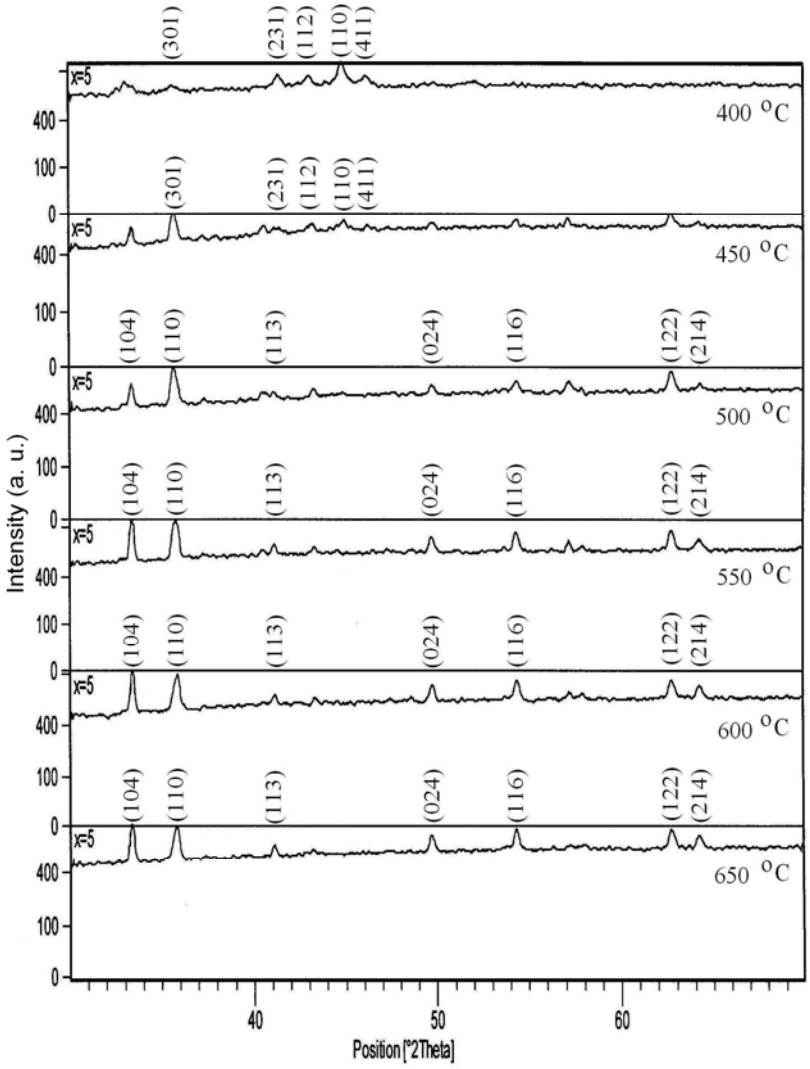

Figure 5.6. XRD for $Fe_{71.25}V_{3.75}P_{15}C_{10}$ powder sample at annealing temperatures from 400 °C to 650 °C for 30 minutes annealing time

This behavior is an agreement with [2]. The linear increase of the lattice parameter of these alloys with increasing V content suggests a simple dilution process. When we increase the temperature from 400 °C to 450 °C, we observe that the intensity of the (110) plane decreases and simultaneously some new peaks of very low intensity are generated. These new diffraction peaks are identified as (113), (024), (116), (122), (214) and (300) at around 41°, 50° , 54°, 57°, 62° and 64° respectively [3]. From 450 °C to 650 °C these peaks increased in amplitude. This indicates a structural change of the samples from 500 °C to higher temperatures.

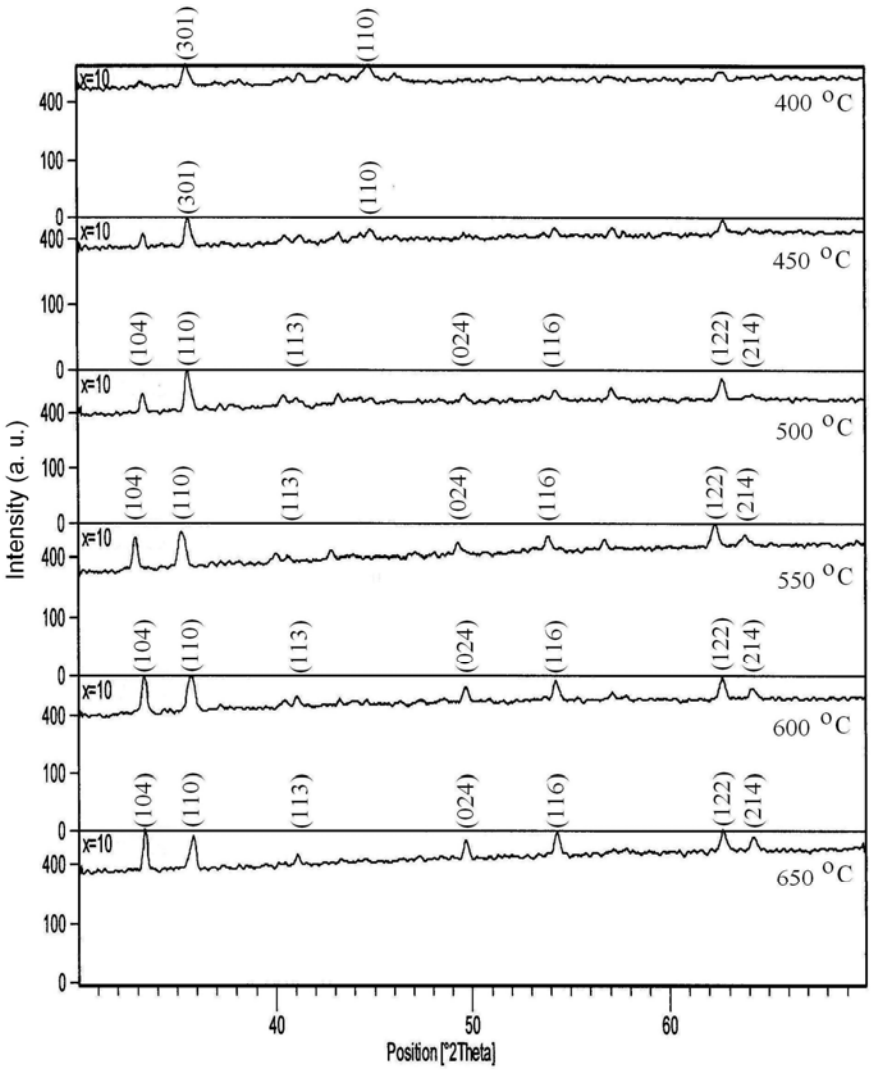

Figure 5.7. XRD for $Fe_{67.5}V_{7.5}P_{15}C_{10}$ powder sample at annealing temperatures from 400 °C to 650 °C for 30 minutes annealing time

The structure of these alloys is consistent with a hexagonal structure (JCPDS card No. 80-0042) and with the XRD machine code reference 76-0182. The lattice parameters (a and c) of this structure were calculated for the planes (116) and (214). The lattice parameters (a and c) of the hexagonal structure were calculated by using the following formula [1].

$$\frac{1}{d_{hkl}^{2}} = \frac{4(h^2 + hk + k^2)}{3a^2} + \frac{l^2}{c^2} \qquad (5.2)$$

Where, h, k and l are the indices of the crystalline plane.

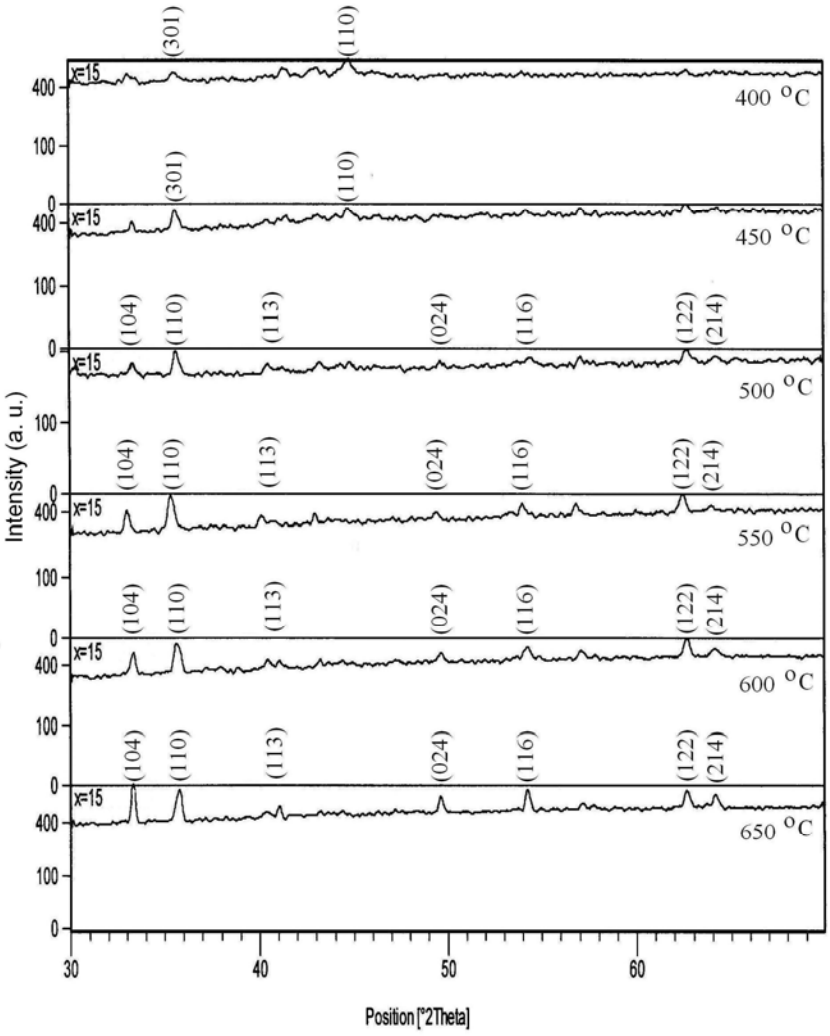

Figure 5.8. XRD for $Fe_{63.75}V_{11.25}P_{15}C_{10}$ powder sample at annealing temperatures from 400 °C to 650 °C for 30 minutes annealing time

For the hexagonal structure the lattice parameter 'a' is almost constant (~ 5.023 Å) for all samples whereas the lattice parameter 'c' increases linearly with the increase of V content in the temperature range 500 °C to 650 °C as shown in table 5.1. At 500 °C the lattice parameter 'c' of the samples taken from the (116) plane is 13.678 Å, 13.697Å, 13.725 Å and 13.725 Å and at 550 °C it is 13.682 Å, 13.704 Å, 13.803 Å and 13.808 Å for x=0, 5, 10 and 15 respectively. On the other hand, at 600 °C the lattice parameter 'c' from the (116) plane is 13.676 Å, 13.682 Å, 13.709 Å and 13.707 Å and at 650 °C it is 13.684 Å, 13.690 Å, 13.705 Å and 13.713 Å for x=0, 5, 10 and 15, respectively. The transformation of the amorphous alloy to the crystalline phases takes place by the nucleation and growth processes. A similar mechanism has also been reported in various amorphous alloys [4-8]. We have observed that the onset of crystalline phase begins from 400 °C for 30 minutes annealing time. These results correspond well with the crystallization temperature as measured in the DTA.

5.3 Grain sizes

The grain size of the powder samples was estimated from the broadening of the highest intensity peak (110) for BCC structure and (116) and (214) peaks for hexagonal structure of the XRD pattern by using the following Scherrer formula [9].

$$L = \frac{0.9 \times \lambda}{(B - 0.05) \times \cos\theta} \qquad (5.3)$$

Where L is the grain size, λ the wavelength of the CuKα radiation (λ=1.54178 Å), 0.05 is the instrumentation broadening, B is the full width at half-maximum (FWHM) of a diffraction peak expressed in radians and θ is the Bragg angle.

The grain size of the samples of $(Fe_{100-x}V_x)_{75}P_{15}C_{10}$ (x=0, 5, 10 and 15) was calculated at annealing temperatures of 400 °C, 450 °C, 500 °C, 550 °C, 600 °C and 650 °C for 30 minutes annealing time. The grain size of the annealed $(Fe_{100-x}V_x)_{75}P_{15}C_{10}$ (x=0, 5, 10 and 15) sample is tabulated in table 5.1. The grain size was 20-52 nm, 16-52 nm, 10-48 nm, 40-48 nm, 26-61 nm and 40-54 nm for annealing temperatures of 400 °C, 450 °C, 500 °C, 550 °C, 600 °C and 650 °C respectively. So, the grain size is dependent on the annealing temperature.

Table 5.1. Lattice parameters and grain size at annealing temperatures from 400 °C to 650 °C for 30 minutes annealing time of the $(Fe_{100-x}V_x)_{75}P_{15}C_{10}$ (x=0, 5, 10 and 15) powder samples

Sample x	Planes (hkl)	Temp. T (°C)	Latt. par. a (Å)	Latt. par. c (Å)	Grain size (nm)
0	110	400	2.854		52
5			2.859		38
10			2.865		32
15			2.870		20
0	110	450	2.853		52
5			2.854		20
10			2.858		28
15			2.858		16
0	116 & 214	500	5.016	13.678	15
5			5.013	13.697	48
10			5.015	13.725	48
15			5.015	13.725	10
0	116 & 214	550	5.040	13.682	40
5			5.018	13.704	48
10			5.045	13.822	48
15			5.027	13.808	48
0	116 & 214	600	5.011	13.676	34
5			5.022	13.682	61
10			5.023	13.709	40
15			5.023	13.707	26
0	116 & 214	650	5.022	13.684	40
5			5.023	13.690	54
10			5.021	13.705	54
15			5.024	13.713	43

5.4 DTA, TGA, DTG of the as prepared samples

DTA techniques are the most frequently used method to study the crystallization behavior. The transition temperature of the samples was monitored by a differential thermal analyzer [Seiko-Ex-STAR-6300, Japan]. The measurements of DTA, TG and DTG were carried out from 40 to 600 °C at a heating rate of 20 °C min^{-1} under nitrogen gas flow. Figures (5.9-5.12) shows the DTA, TG% and DTG curve of the as prepared samples. In the DTA curve only one exothermic peak occurred for each sample at around 400 °C. The peak of each sample is attributed to the crystallization temperature. Crystallization temperature increases with the increase of V content in the as prepared $(Fe_{100-x}V_x)_{75}P_{15}C_{10}$ (x=0, 5, 10 and 15) samples. This is due to the crystallization temperature of V is higher than the crystallization temperature of Fe.

In the TG curve, it has observed that mass is slightly gained for all samples. Passively, as the temperature is increased the micro voids which formed during the growth process of the ribbon during melt spinning are gradually eliminated. Then at higher temperatures Fe and V ions absorb oxygen from the environment and hence the mass could be slightly enhanced. This mass gain had been also founded in TG measurement of different compositions of $(Fe_{100-x}Mn_x)_{75}P_{15}C_{10}$ amorphous ribbons [10]. Crystallization temperature and TG% of the as prepared samples of $(Fe_{100-x}V_x)_{75}P_{15}C_{10}$ (x=0, 5, 10 and 15) are given in table 5.2.

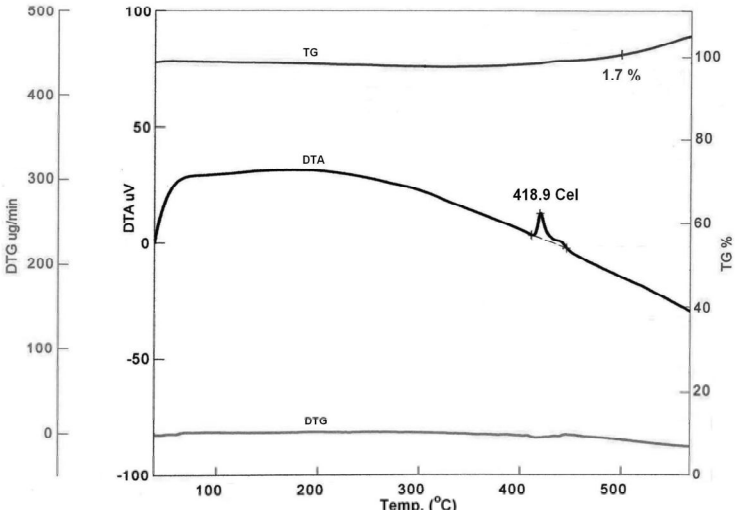

Figure 5.9. DTA, TG% and DTG of the as prepared $Fe_{75}P_{15}C_{10}$ ribbon

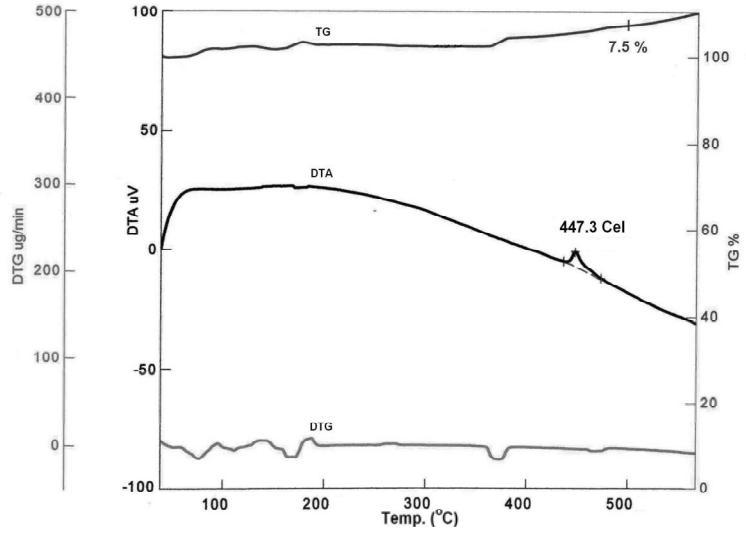

Figure 5.10. DTA, TG% and DTG of the as prepared $Fe_{71.25}V_{3.75}P_{15}C_{10}$ ribbon

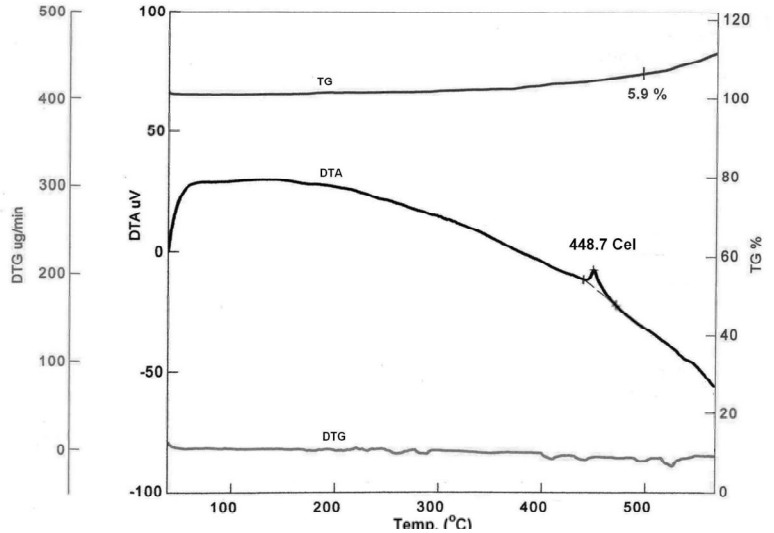

Figure 5.11. DTA, TG% and DTG of the as prepared $Fe_{67.5}V_{7.5}P_{15}C_{10}$ ribbon

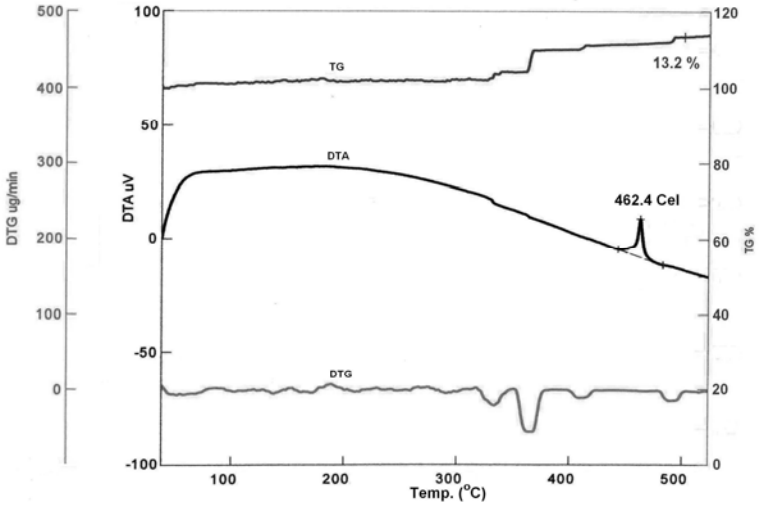

Figure 5.12. DTA, TG% and DTG of the as prepared $Fe_{63.75}V_{11.25}P_{15}C_{10}$ ribbon

Table 5.2. Crystallization temperature (T_x) and TG% of the as prepared $(Fe_{100-x}V_x)_{75}P_{15}C_{10}$ (x=0, 5, 10 and 15) ribbons

Samples, x	T_x (°C)	TG % at 500 °C
0	418.9	1.7
5	447.3	7.5
10	448.7	5.9
15	462.4	13.2

Crystallization temperature as a function of x [%] of $(Fe_{100-x}V_x)_{75}P_{15}C_{10}$ is shown in figure 5.13. From figure we see that crystallization temperature vary linearly with the V composition.

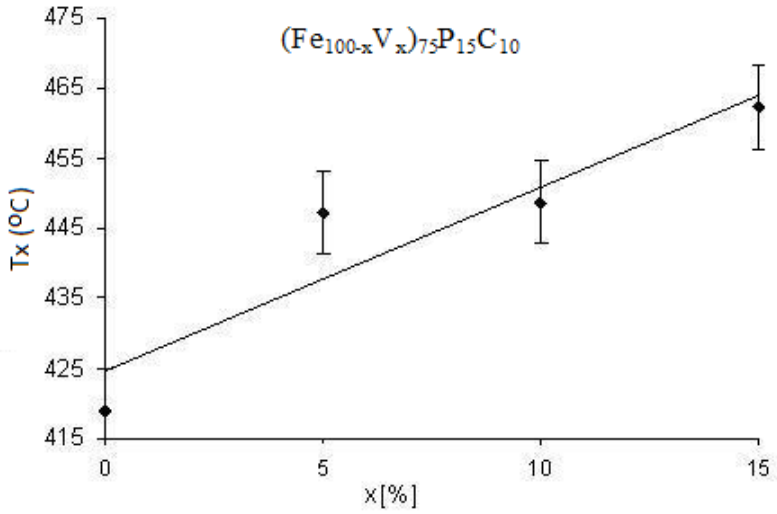

Figure 5.13. Crystallization temperature (T_x) as a function of x [%] of the as prepared $(Fe_{100-x}V_x)_{75}P_{15}C_{10}$ (x=0, 5, 10 and 15) ribbons

In the DTG curves some small peaks are found for the samples x=5 and 10 which means that there is a small change of mass, but for x=15 some broad peaks are found which indicates that there is large change of mass, within small ranges of the heating temperature.

5.5 Surface micrographs of the as prepared samples

Hitachi S-3400N variable pressure SEM was used for surface morphology. Surface micrographs of as prepared samples are shown in figures (5.14-5.17). For the purpose of Fe-V-P-C alloy Fe, V, P and C were kept in a quartz tube in their stoichiometric ratio and the melt of the composition is kept above the melting point of alloy until a homogeneous mixing in obtained. The molten alloy flow through the outlet of the quartz tube and it is cooled at an ultra fast rate (~10^6 ˚C/min) with the help of a rotating cooled copper cylinder. So, after melting the atoms of different composition were kept in random orientation. SEM image of as prepared sample shows of this random orientation of the molted atoms. From the micrographs, we have observed some black dots that indicate the pore in the micrographs.

These acute sizes of pore are observed in the alloy due to rapid cooling of the molten alloy and very high Cu spinning (~ 6000 rev/min). With the increases of V content into the samples, the concentration fluctuations increase while the porosity decreases. With the increase of V content into the samples the malleability of the samples increases. The non magnetic atoms of P and C are glass forming materials which changes the physical properties of the ribbon i.e., elasticity, softness, etc. It also influences the grain size of the annealed samples. Micrographs of the annealed sample could not be studied because of the low resolution of the SEM machine. It needs TEM for the study of annealed samples.

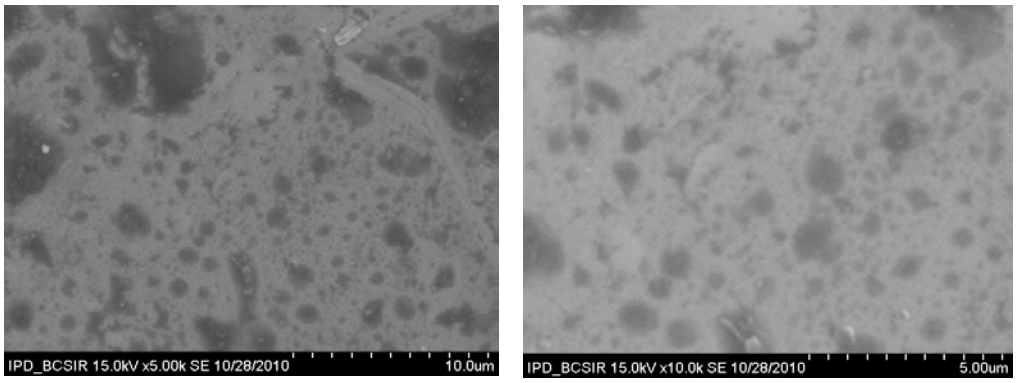

(i) Resolution 5000 (ii) Resolution 10000

Figure 5.14. Surface micrographs of the as prepared $Fe_{75}P_{15}C_{10}$ ribbon at resolutions (i) 5000 (ii) 10000

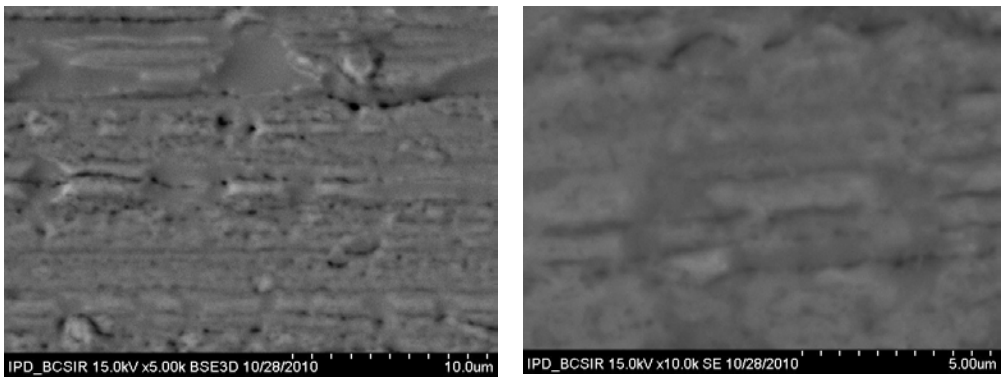

(i) Resolution 5000 (ii) Resolution 10000

Figure 5.15. Surface micrographs of the as prepared $Fe_{71.25}V_{3.75}P_{15}C_{10}$ ribbon at resolutions (i) 5000 (ii) 10000

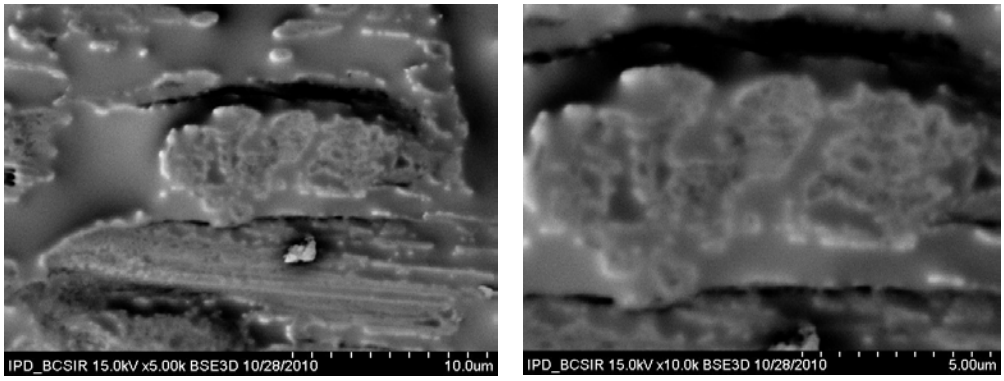

(i) Resolution 5000 (ii) Resolution 10000

Figure 5.16. Surface micrographs of the as prepared $Fe_{67.5}V_{7.5}P_{15}C_{10}$ ribbon at resolutions (i) 5000 (ii) 10000

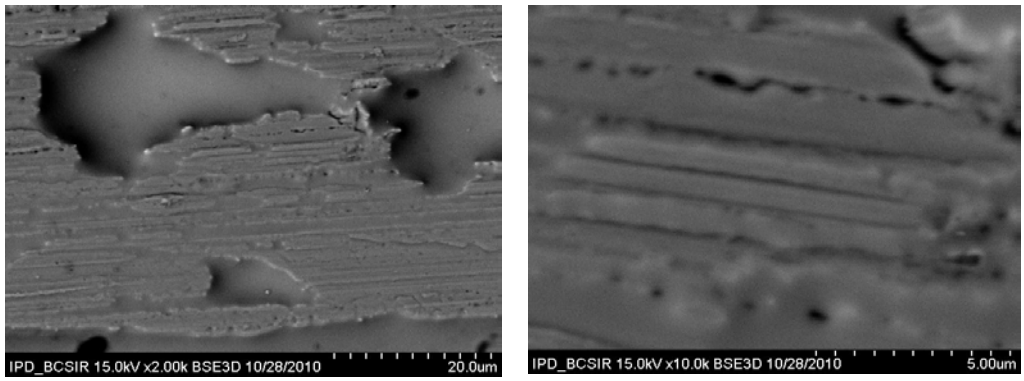

(i) Resolution 2000 (ii) Resolution 10000

Figure 5.17. Surface micrographs of the as prepared $Fe_{63.75}V_{11.25}P_{15}C_{10}$ ribbon at resolutions (i) 2000 (ii) 10000

5.6 Resistivity of the as prepared samples at room temperature

Figure 5.18 shows the resistivity with V content at room temperature (298 K) of the as prepared samples of $(Fe_{100-x}V_x)_{75}P_{15}C_{10}$ (x=0, 5, 10 and 15). The resistivity of the samples increases with the increase of V content at room temperature. Resistivity of different samples is also shown in table 5.3. Isotropic and anisotropic spin scattering mechanisms contribute to the resistivity in magnetically ordered amorphous metals [11-15]. For the scattering centers, magnons and magnetic impurities have been proposed for the increase of resistivity [16]. In some cases, the structural disorder of the atomic sites introducing magnetic scattering to the resistivity [17]. Topological spin disorders are also thought to be responsible for the increase of resistivity.

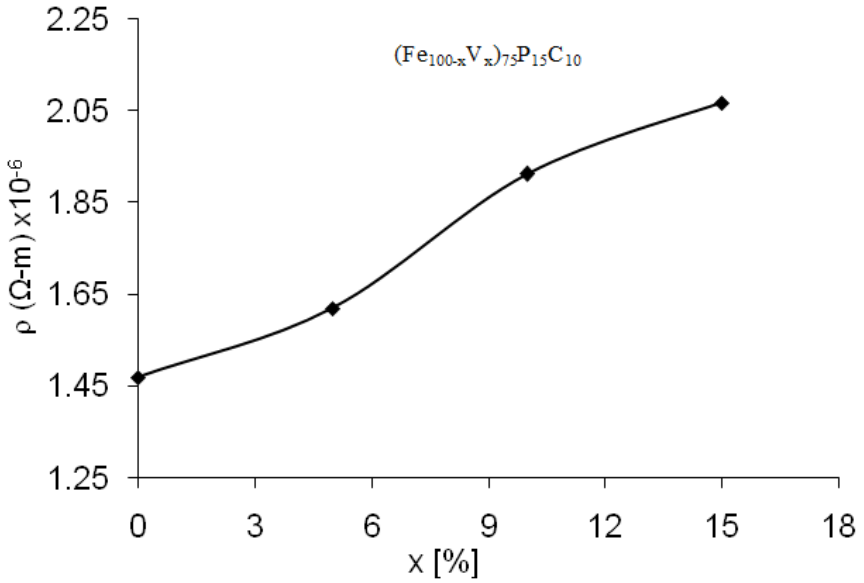

Figure 5.18. Resistivity as a function of x [%] of the as prepared $(Fe_{100-x}V_x)_{75}P_{15}C_{10}$ (x=0, 5, 10 and 15) ribbons at room temperature

Table 5.3. Resistivity of the as prepared $(Fe_{100-x}V_x)_{75}P_{15}C_{10}$ (x=0, 5, 10 and 15) ribbons at room temperature

Samples, x	Resistivity, ρ (Ω-m)×10^{-6}
0	1.41
5	1.60
10	1.91
15	2.06

5.7 Temperature dependent of normalized resistivity of the as prepared samples

Figure 5.19 shows the temperature dependent of normalized resistivity of the as prepared samples. Resistivity decreases with the decrease in temperature for sample x=0 and 5. This may be happening due to the decrease of incoherent electron-magnon scattering. In the case of x=10, 15 the resistivity increases with the decrease in temperature. This is due to the structural topological scattering. The TCR is positive for sample x=0, 5 while TCR negative for samples x=10, 15. These results follow the Mooij-correlation [18] of metallic glasses which is based on quantum mechanical coherence effects, namely incipient Anderson localization [19].

This correlation states that if the resistivity of amorphous alloys with d-bands is greater than the saturation value $\rho^* \approx 160$ μΩ-cm, TCR is negative and it changes to positive values when $\rho < \rho^*$. For the sample x=0 and 5 the measured resistivity at room temperature was 141 μΩ-cm and 160 μΩ-cm respectively that show positive TCR. On the other hand, for the sample x=10 and 15 the measured resistivity at room temperature was 191 μΩ-cm and 206 μΩ-cm respectively that show negative TCR. Such transport phenomena deviates from the conventional Boltzmann's transport.

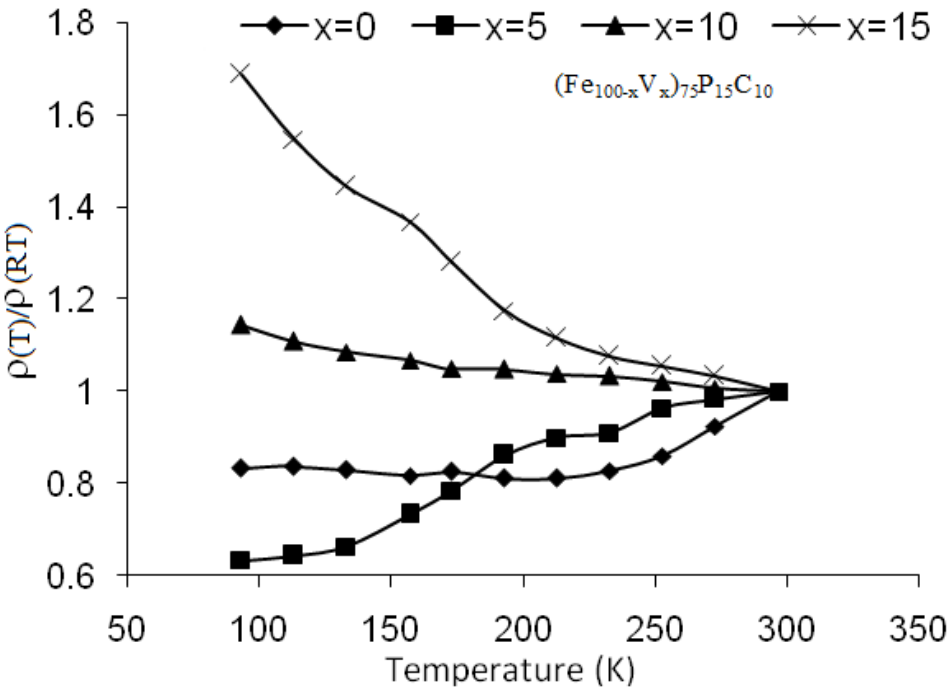

Figure 5.19. Temperature dependent of normalized resistivity of the as prepared $(Fe_{100-x}V_x)_{75}P_{15}C_{10}$ (x=0, 5, 10 and 15) ribbons

In the case of disorder metals, the wavelength of the conduction electron is comparable with the atomic distances which result in interference between scattering waves. The negative TCR is the result of reduction of interferences with temperature rises. Again, the gradual change from positive TCR to negative TCR with V content is accompanied by shortening of the mean free path down to an average atomic distance. An increase in resistivity in this regime is due entirely to the mean free path effect and is free from the band structure effect.

5.8 Magnetoresistance (MR) of the as prepared samples at room temperature

The MR measurement of the as prepared samples was carried out by measuring current, applied magnetic field and the developing voltage at room temperature. The magnetic field is applied to the perpendicular of current. The MR of the as prepared samples was calculated by using the following formula [20].

$$MR\% = \frac{R(H) - R(0)}{R(0)} \times 100\% \qquad (5.4)$$

Where, R(H) is the resistance in presence of magnetic field and R(0) is the resistance in the absence of magnetic field.

Figure 5.20 shows the MR% of the as prepared samples at room temperature for different V content as a function of magnetic field upto 0.6 T.

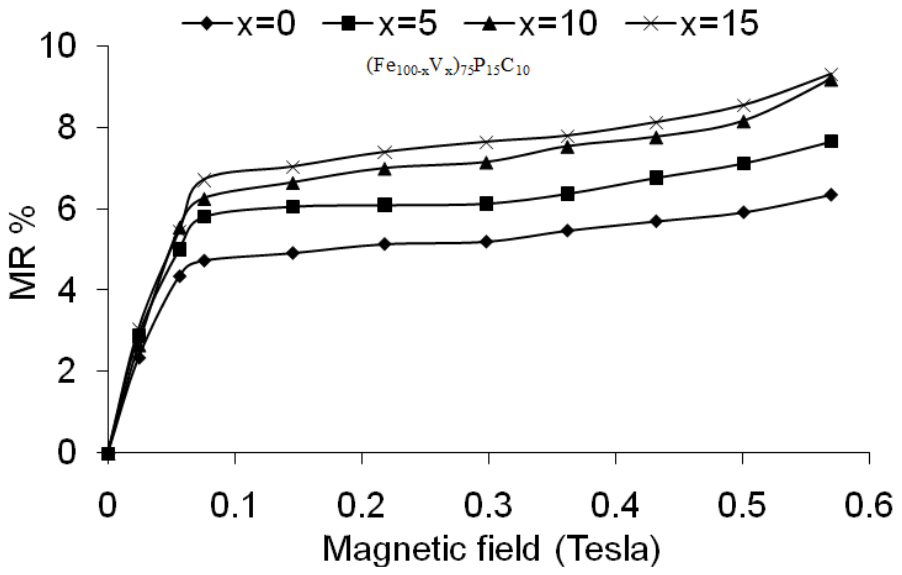

Figure 5.20. Variation of MR with applied field of the as prepared $(Fe_{100-x}V_x)_{75}P_{15}C_{10}$ (x=0, 5, 10 and 15) ribbons at room temperature

An initial large change in resistivity is accompanied by growth of magnetic domain parallel to the direction of the magnetic field. Once the magnetic saturation is achieved there is no domain motion as it becomes a single domain.

The only contribution to the MR comes at this stage is from the conduction electron scattering due to the collision between themselves and hence the electron mean free-path is much longer in this stage. The physical origin of the MR effect lies in spin orbit coupling. As magnetic moment rotates, the electron cloud about each nucleus deforms slightly and this deformation changes the amount of scattering undergone by the conduction electrons in their passage through the lattice. It is seen from the figure that MR% increases with increase of V content. If V content increases, the topological spin disorder increases in the system and hence MR% increases. The MR varies from 0 to 8% with the increase of V content and also with the applied magnetic field.

5.9 Hall resistivity of the as prepared samples at room temperature

Figure 5.21 shows the Hall resistivity as a function of magnetic field of the as prepared samples at room temperature. It is seen that the Hall resistivity initially increases very rapidly and then saturates with the applied magnetic field. Hall resistivity also increases with the increase of V content. Once saturation is achieved there is no domain motion as it has assumed a single domain.

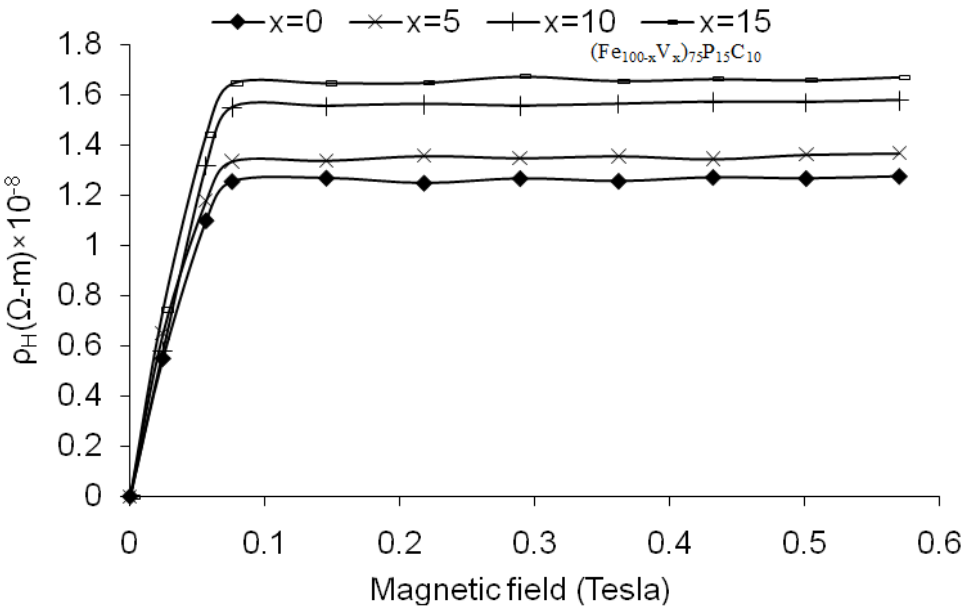

Figure 5.21. Hall resistivity as a function of magnetic field of the as prepared $(Fe_{100-x}V_x)_{75}P_{15}C_{10}$ (x=0, 5, 10 and 15) ribbons at room temperature

One must consider the quantum mechanical side jump mechanism [21] according to which the electrons a small transverse deflection at each scattering event. If this mechanism were dominant in our alloys, ρ_H should be proportional to ρ^2. While the V content increase in the alloys, magnetic impurities and also topological spin disorder increases that may be responsible for the increase of Hall resistivity. One or more of the scattering processes i. e. impurity, phonon and spin disorder scattering give dominant contribution to the anomalous Hall effect in different filed which, in turn, are different for different samples. The anomalous Hall effect results from anisotropic scattering and this in turn comes from an interplay of internal polarization, (spin) scattering centers and spin-orbit coupling. The internal polarization can be provided by the spontaneous magnetization inside a domain or by an induced magnetization. The non linear behavior of the ρ_H vs $\mu_0 H$ curve decomposed into the normal Hall effect and anomalous Hall effect that can be written are as follows [19].

$$\rho_H = R_0 \mu_0 H + R_s M_s \tag{5.5}$$

The first term, characterized by the ordinary Hall coefficient (R_0) and the second term characterized by the extraordinary or anomalous Hall coefficient (R_s). From this figure we have seen that there is a saturation in the ferromagnetic regime always, indicating that the anomalous Hall effect dominates. This is not found in equivalent crystalline materials [22]. As elementary anisotropic scattering mechanisms, so far, the quasi-classical skew scattering (first order [23]) and the quantum mechanical (second order) side jump have been proposed. These mechanisms have been investigated in relation to certain (spin) scattering centers, such as spin waves [23] or spin impurities [24], but apparently other possible spin scattering centers have not been covered as yet. Accordingly, the anomalous Hall constant, $R_s = c_1\rho + c_2\rho^2$ have been proposed [25], where $c_{1,\ 2}$ are supposed to refer to the first order (skew) and second order (side jump) mechanisms. For amorphous systems often it is argued that because of the large number of scattering centers the quadratic term should dominate and since the side jump supposedly does not depend very much on the type of scattering potential, it has deal with the same scattering situation in case of ρ and ρ_H and therefore $\rho_H \sim \rho^2$ might be valid [26].

5.10 DC magnetization of the as prepared samples at room temperature

The DC magnetization as a function of applied magnetic field of the as prepared $(Fe_{100-x}V_x)_{75}P_{15}C_{10}$ (x=0, 5, 10 and 15) samples was measured at room temperature (298K) is shown in figure 5.22. The magnetization of all samples increases linearly with increasing the applied magnetic field up to 0.5 kG. Beyond this field magnetization increases slowly and then saturation occurs. Therefore, it is clear that at room temperature all samples are in ferromagnetic state. When a magnetic field is applied, the magnetic domains align along the field direction and the magnetization saturates, here for relatively low applied fields. The saturation magnetization is decreases with increase of V content.

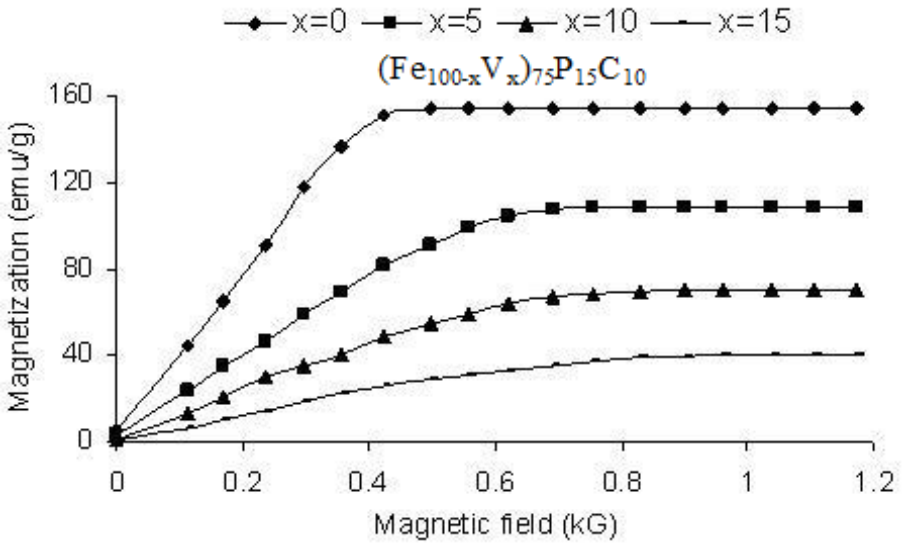

Figure 5.22. DC magnetization as a function of magnetic field of the as prepared $(Fe_{100-x}V_x)_{75}P_{15}C_{10}$ (x=0, 5, 10 and 15) ribbons at room temperature

The saturation magnetization (M_s) and Bohr magneton (μ_B) per Fe atom of the as prepared $(Fe_{100-x}V_x)_{75}P_{15}C_{10}$ (x=0, 5, 10 and 15) samples at room temperature are shown in table 5.4. Bohr magneton per formula of $(Fe_{100-x}V_x)_{75}P_{15}C_{10}$ (x=0, 5, 10 and 15) samples can be obtained by using the following formula [27].

$$\mu_B = \frac{M}{5585} \times Ms \qquad (5.6)$$

Where, M is the molecular weight of the substance and M_s is the saturation magnetization.

Table 5.4. Saturation magnetization and Bohr magneton of the as prepared $(Fe_{100-x}V_x)_{75}P_{15}C_{10}$ (x=0, 5, 10 and 15) ribbons at room temperature

Samples, x	Saturation magnetization M_s (emu/g)	Bohr magneton (μ_B) per Fe atom
0	154	1.275
5	109	0.894
10	70	0.573
15	40	0.328

Figure 5.23 shows the saturation magnetization as a function of V content. The decrease of saturation magnetization and hence the Bohr magneton is due to the replacement of ferromagnetic Fe by paramagnetic V. This reduction also happened due to the overall interatomic exchange interaction of the Fe atoms. The value of saturation magnetization is consistent with the literature value [28].

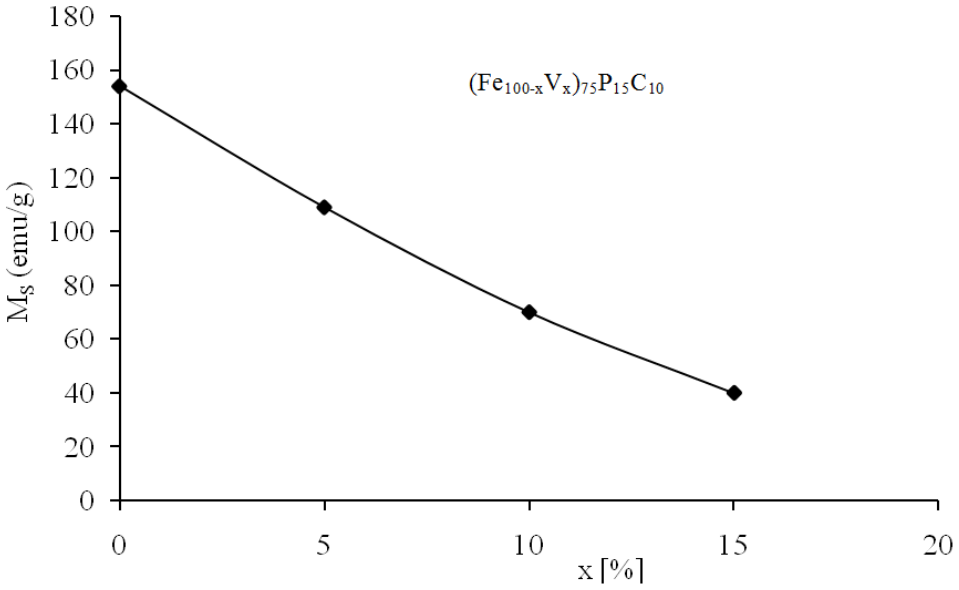

Figure 5.23. Saturation magnetization as a function of x [%] of the as prepared $(Fe_{100-x}V_x)_{75}P_{15}C_{10}$ (x=0, 5, 10 and 15) ribbons at room temperature

References

[1] Kittel, C., "Introduction to solid state physics", 7th edition, John Wiley & Sons, Inc., Singapore, 1996.

[2] Al-Omari, I. A., and Hamdeh, H. H., "Mossbauer and structural studies of $Fe_{0.7-x}V_x\ Si_{0.3}$", Phys. Stat. Sol. (c), 7, 1809-1812, 2004.

[3] Cuiling, G., Wenli, Z., Hongbian L., Leiming, L., and Zheng, X., "Controllable fabrication of mesoporous MgO with various morphologies and their absorption performance for toxic pollutants in water", Crys. Grow. & Desi., 8, 3785-3790, 2008.

[4] Mader, S., "Crystallization behavior of an amorphous Fe-P-C alloy" J. Vac. Sci. & Teeh., 2, 35-41, 1965.

[5] Idem, in "Recrystallization, grain growth and texture", American Society of Metals, Ohio, p.523, 1966.

[6] Crewdson, R. C., Ph. D. Thesis, California Institute of Technology, Pasadena, California, 1966.

[7] Duwez, P., in "Phase stability in metals and alloys", Ed. Rudman, P. S., Stringer, J., and Jaffee, R. I., McGraw-Hill, New York, p.523, 1967.

[8] Bagley, B. G., and Turnbull, D., "The preparation and crystallization behavior of amorphous nickel-phosphorus thin films", Acta Metallurgica, 18, 857-858, 1970.

[9] Klue, H. P., Alexander, L. E., "X-ray diffraction procedures for polycrystalline and amorphous materials", John Wiley & Sons, New York, p. 627, 1997.

[10] Kamruzzaman, M., M. Phil. Thesis in Physics, BUET, 2010.

[11] Heinemann, K., and Barner, K., "Magnetic field sensor for cryogenic applications", J. Appl. Phys. Lett. 50, 1284-1285, 1987.

[12] Cote, P. J., and Meisel, L.V., Glassy Metals I, eds. Guntherrodt, H. J., and Beck, H., Spinger Verlag, Berlin, p.141, 1981.

[13] Sinha, A. K., "Temperature and field dependence of magnetization of amorphous (Fe, Mn)-P-C alloys", J. Appl. Phys., 42, 338, 1971.

[14] Heinemann, K., Ph. D. Thesis**,** University of Göttingen, Germany, 1987.

[15] Kaul, S. N., Kettlerr, W., and Rosenberg, M., "Evidence for a magnetic contribution to the electrical resistivity in amorphous $Fe_{80}B_{20-x}C_x$ alloys", Phys Revs. B, 33, 4987-4997, 1986.

[16] Kaul, S. N., "Anomalous Hall effect in nickel and nickel-rich nickel-copper alloys", Phys. Rev. B, 20, 5122-5130, 1979.

[17] Erle, A. and Barner, K., “High pressure resistivity of MnAs”, J. Magn. Matter., 74(2), 225-230, 1988.

[18] Mooij, J. H., “Electrical conduction in concentrated disordered transition metal alloys”, Phys. Status Solidi (a), 17, 521-530, 1973.

[19] Mizutani, U., “Introduction to the electron theory of metals”, Cambridge University Press, p. 483, 2001.

[20] Cullity, B. D., “Introduction to magnetic materials” Addition-Wisley publishing company, Inc., California, 1972.

[21] Berger, L., “Side jump mechanism for the Hall effect of ferromagnet”, Phys. Rev. B, 2, 4559-4566, 1970.

[22] Hurd, C. M., “The Hall effect in metals and alloys”, Plenum Press, New York, 1972.

[23] Kondo, J., “Anomalous Hall effect and magnetoresistance of ferromagnetic metals”, Prob. Theor. Phys., 27, 773-793, 1962.

[24] Berger, L., “Side-jump mechanism for the Hall effect of ferromagnets”, Phys. Rev. B, 2, 4559-4566, 1970.

[25] Luttinger, J. M., “Hall effect in ferromagnetics”, Phys. Rev., 95, 1154-1160, 1954.

[26] Hasegawa, R., and Dermon, J. A., “Electrical resistivity and Curie temperature of amorphous (Fe-Ni)-P-C alloys”, Phys. Lett. A, 42, 407-409, 1973.

[27] Tsuei, C. C., and Lilienthal, H., “Magnetic distribution in an amorphous ferromagnet”, Phys. Rev. B, 13, 4899-4906, 1976.

[28] Smit, J., “Magnetic properties of material”, McGraw-Hill, New York, 1971.

CHAPTER 6
CONCLUSIONS

6.1 Conclusions

The results of the structural, thermal, transport and magnetic properties of the melt-spun $(Fe_{100-x}V_x)_{75}P_{15}C_{10}$ (x=0, 5, 10 and 15) amorphous ribbons are summarized and the following conclusive statements can be made from this research work.

XRD patterns of the as prepared samples show that each sample contains a broad peak which confirms the samples are amorphous in nature. The re-crystallization phenomenon of the alloys was studied by XRD for annealing temperatures from 400 °C to 650 °C within 30 minutes annealing time. The BCC structure was observed for the temperatures from 400 °C to 450 °C while the hexagonal structure for temperatures from 500 °C to 650 °C. The lattice parameter 'a' of the BCC structure was calculated for (110) plane and it changes from 2.854 Å to 2.870 Å. The lattice parameters 'a' and 'c' of the hexagonal structure were calculated for the planes (116) and (214). The lattice parameter 'a' is almost constant (~ 5.023 Å) for all samples whereas the lattice parameter 'c' changes from 13.676 Å to 13.822 Å. The transformation of the amorphous alloy to the crystalline phases takes place by the nucleation and growth processes. The crystalline grain size of the samples was estimated by using the Scherrer formula and is found to vary from 10 nm to 60 nm in the annealing temperature from 400 °C to 650 °C for 30 minutes annealing time.

In DTA curve of the as prepared samples shows an exothermic peak for each sample and these peak values increases with increase of V content which attributed to the crystallization temperature. The crystallization temperatures are 418.9 °C, 447.3 °C, 448.7 °C and 462.4 °C for x=0, 5, 10 and 15 respectively. Crystallization temperature increases with increase of V content because the melting point of V is higher than Fe. TG% curve shows that as the temperature increases, mass is slightly gained for all samples. At higher temperature Fe and V ions absorb oxygen from the experimental environment and hence mass are slightly gained at higher temperature. The volume/grain increases also with the increase of the V content because the ionic radius of V (1.92 Å) is larger than the ionic radius of Fe (1.72 Å).

In the DTG curves some small peaks are found for the samples x=5 and 10 which means that there is a small change of mass, but for x=15 some broad peaks are found which indicates that there is large change of mass, within small ranges of the heating temperature.

Surface micrograph of the as prepared samples was measured by the scanning electron microscope. It shows that the concentrations fluctuation increases with the increase of V content into the samples. This also shows that the porosity decreases with the increase of V content. Micrographs of the annealed sample could not be studied because of the low resolution of the SEM machine. It needs TEM for the study of grain sizes of the annealed samples.

Resistivity of the as prepared samples at room temperature increases with the increase of V content in the system due to the magnetic impurities, scattering and topological spin disorder. For the samples x=0 and 5 the measured resistivity at room temperature was 141 μΩ-cm and 160 μΩ-cm respectively that show positive TCR. For the samples x=10 and 15 the measured resistivity at room temperature was 191 μΩ-cm and 206 μΩ-cm respectively that show negative TCR. These results follow the Mooij-correlation of metallic glasses. Such transport phenomena deviates from the conventional Boltzmann's transport. The resistivity of metallic amorphous alloys can also explain by the Ziman-Faber model, which is an expansion of the Ziman model for the resistivity measurement of non-magnetic liquid (amorphous) metals. In this approach the scattering is related to the structure factor; in particular, the resistivity is considered to be a weighted integral of the structure factor, with integration up to the Fermi surface. This model or extensions of it is also used to explain the Mooij-correlation, i.e. the empirically observed correlation between the absolute value of the resistivity and its temperature derivative.

The initial large change in the MR of the as prepared samples at room temperature occurs in the low field due to the growth of magnetic domain parallel to the direction of the magnetic field. Once the magnetic saturation is achieved there is no domain motion as it has assumed a single domain. The only contribution to the MR comes at this stage is from the conduction electron scattering.

The electron mean free path is much longer in this stage. The MR varies from 0 to 8 % with the applied magnetic field. MR% also increases with the increase of V content because as V content increase into the alloy the topological disorder increases.

Hall resistivity of the as prepared samples at room temperature increases with the increase of applied magnetic field and also V content. The non linear behavior of the ρ_H vs B curve indicates that the samples show the anomalous Hall effect. One or more of the scattering processes i. e., impurity, phonon and spin disorder scattering give dominant contribution to the anomalous Hall effect. While the V content increases, magnetic impurities and also topological spin disorder increases that may be responsible for the increase of Hall resistivity. The skew-scattering and the side-jump mechanism also responsible for anomalous Hall effect.

The saturation magnetization of the as prepared samples at room temperature are 154, 109, 70 and 40 emu/g for x=0, 5, 10 and 15 respectively. The saturation magnetization decreases with the increase of V content of the samples. This decrease is due to the replacement of ferromagnetic Fe by paramagnetic V and also due to the reduction of the overall interatomic exchange interaction. Hence, the Bohr magneton for x=0, 5, 10, 15 are 1.275, 0.894, 0.573 and 0.328 per Fe atom in the samples respectively.

PUBLICATIONS

Indexed Journal

1) M. A. S. Karal, K. Bärner, M. Kamruzzaman, D. K. Saha, and F. A. Khan, Recrystallization phenomenon in melt-spun $(Fe_{100-x}V_x)_{75}P_{15}C_{10}$ alloys, Int. J. Basic and Applied Sciences, 11(1), 54-58, 2011

2) M. A. S. Karal, M. Kamruzzaman, M. G. M. Hossain, H. M. I. Jaim F. A. Khan; Transport, magnetic and thermal properties of $(Fe_{100-x}V_x)_{75}P_{15}C_{10}$ semi-amorphous ribbons, The Nucleus, 48(2), 83-89, 2011

3) M. A. S. Karal, M. Kamruzzaman, D. K. Saha and F. A. Khan; Characterization of amorphous $Fe_{69}V_6P_{15}C_{10}$ metallic alloy (**Accepted,** Bangladesh Journal of Physics)

Proceedings

1) M. A. S. Karal, M. G. M. Hossain, M. Kamruzzaman, H. M. I. Jaim and F. A. Khan; Magnetization, magnetoresistance and Hall resistivity of $(Fe_{100-x}V_x)_{75}$ $P_{15}C_{10}$ amorphous ribbons, Proceedings in the 3rd Int. conf. on Structure, Processing and Properties of Materials (SPPM-2010), 24-26 February 2010, Co-operated by MRS, USA. (Oral Presentation)

2) M. A. S. Karal, M. Kamruzzaman, M. G. M. Hossain, H. M. I. Jaim and F. A. Khan; Resistivity, magnetoresistance and magnetization measurement of $(Fe_{100-x}V_x)_{75}$ $P_{15}C_{10}$ amorphous ribbons, Proceeding in the Int. conf. on Magnetism and Advanced Materials (ICMAM-2010), 03-07 March 2010, Sponsored by Int. Sci. Programme (ISP), Uppsala University, Sweden, p. 68 (Oral Presentation)

3) M. A. S. Karal, M. Kamruzzaman, M. G. M. Hossain, H. M. I. Jaim and F. A. Khan; Transport, magnetic and thermal properties of $(Fe_{100-x}V_x)_{75}$ $P_{15}C_{10}$ alloys, Proceedings in the (Abstract- POS 28-3) Int. conf. on Recent Advances in Physics (RAP-2010), 27-29 March, 2010; Organized by Department of Physics, University of Dhaka, Bangladesh, p.70 (Poster Presentation)

4) M. A. S. Karal, M. Kamruzzaman, D. K. Saha and F. A. Khan; Characterization of amorphous $Fe_{69}V_6P_{15}C_{10}$ metallic alloy, Proceedings (Abstract: MS-V-A 12) in the national conference in Physics, Organized by Bangladesh Physical Society, 10-11 February, 2011, p.32 (Oral Presentation)

APPENDIX

Table 1: XRD data for annealing temperature of 400 °C

	x=0			
Position [° 2 Th.]	Height [cts]	FWHM [° 2 Th.]	d-spacing (Å)	Rel. Int. [%]
35.2686	101.15	0.1181	2.54484	40.14
35.6954	113.5	0.3149	2.51539	45.04
41.3167	139.2	0.3149	2.18523	55.24
43.0523	122.2	0.2362	2.10107	48.49
44.861	252.02	0.2165	2.01847	100
46.1369	92.9	0.384	1.9659	36.86
	x=5			
35.7066	59.94	0.4723	2.51463	19.86
41.38	151.76	0.3149	2.18203	50.27
43.0412	130.36	0.3936	2.10159	43.18
44.8257	301.88	0.2755	2.02198	100
46.1492	124.66	0.4723	1.96703	41.3
51.834	36.52	1.152	1.76242	12.1
	x=10			
35.5397	177.2	0.1968	2.52606	100
41.3037	64.62	0.4723	2.18589	36.47
43.0063	46.52	0.9446	2.10321	26.25
44.7335	122.76	0.3149	2.02594	69.28
62.6488	55.62	0.576	1.48168	31.39
	x=15			
35.6231	62.36	0.6298	2.52033	55.68
41.4055	55.12	0.4723	2.18075	49.21
44.7998	112	0.48	2.02942	100

Table 2: XRD data for annealing temperature of 450 °C

	x=0			
Position [° 2 Th.]	Height [cts]	FWHM [° 2 Th.]	d-spacing (Å)	Rel. Int. [%]
35.2686	101.15	0.1181	2.54484	40.14
35.6954	113.5	0.3149	2.51539	45.04
41.3167	139.2	0.3149	2.18523	55.24
43.0523	122.2	0.2362	2.10107	48.49
44.861	252.02	0.2165	2.01747	100
46.1369	92.9	0.384	1.9659	36.86
	x=5			
33.4168	145.44	0.2165	2.68151	58.59
35.7058	248.24	0.2952	2.51468	100
40.6011	77.46	0.3542	2.22208	31.21
43.1721	64.66	0.4723	2.09552	26.05
44.9047	75.4	0.4723	2.01861	30.37
54.3891	61.81	0.4723	1.6869	24.9
57.1872	68.1	0.4723	1.61084	27.43
62.7225	118.91	0.336	1.48011	47.9
	x=10			
33.3671	73.41	0.1968	2.68539	39.14
35.6249	187.55	0.2165	2.52021	100
40.8943	17.64	0.9446	2.20682	9.4
44.8462	60.34	0.3542	2.02111	32.17
57.1615	46.63	0.3542	1.6115	24.86
62.7459	89.41	0.288	1.47962	47.67
	x=15			
33.3237	34.59	0.94446	2.68879	24.91
35.6161	138.89	0.1968	2.52081	100
44.8394	56.06	0.576	2.02105	26

Table 3: XRD data for annealing temperature of 500 °C

	x=0			
Position [° 2 Th.]	Height [cts]	FWHM [° 2 Th.]	d-spacing (Å)	Rel. Int. [%]
33.3812	149.45	0.2362	2.68429	60.53
35.7018	246.89	0.2558	2.51495	100
40.9473	45.67	30.9446	2.20408	18.5
44.8522	72.77	0.4723	2.02085	29.48
54.386	65.21	0.6298	1.68699	26.41
57.1428	71.75	0.3149	1.61198	29.06
62.72	133.06	0.384	1.48017	53.9
	x=5			
33.4222	207.06	0.1968	2.68109	58.88
35.705	351.66	0.2952	2.51474	100
40.8775	48.98	0.9446	2.20769	13.93
43.2861	72.92	0.2362	2.09026	20.74
49.7639	83.96	0.3149	1.83229	23.88
54.3605	106.85	0.2362	1.68772	30.38
57.2025	103.71	0.3149	1.61044	29.49
62.7427	185.9	0.288	1.47969	52.86
	x=10			
33.3367	145.13	0.2165	2.68777	42.8
35.5897	339.07	0.2165	2.52262	100
40.4266	89.65	0.3149	2.23126	26.44
43.2176	73.04	0.2362	2.09342	21.54
49.6384	53.31	0.4723	1.83663	15.72
54.28	80.14	0.2362	1.69004	23.63
57.1207	98.7	0.2362	1.61256	29.11
62.6845	75.26	0.36	1.48092	51.69
	x=15			
33.3638	48.75	0.4723	2.68565	40.54
35.6429	120.24	0.2362	2.51897	100
40.846	20.51	0.9446	2.20932	17.06
54.2841	28.92	0.9446	1.68992	24.05
62.6921	70.94	0.384	1.48076	59

Table 4: XRD data for annealing temperature of 550 °C

	x=0			
Position [° 2 Th.]	Height [cts]	FWHM [° 2 Th.]	d-spacing (Å)	Rel. Int. [%]
32.9826	323.83	0.2165	2.71581	96.29
35.2455	277.6	0.264	2.54435	82.54
35.4216	336.32	0.1771	2.5342	100
40.5637	46.21	0.9446	2.22404	13.74
49.3563	113.73	0.3542	1.84647	33.81
53.9516	167.56	0.2755	1.69254	49.82
57.1098	39.59	0.9446	1.61284	11.77
62.3808	158.33	0.3936	1.48863	47.08
63.8727	78.29	0.576	1.45621	23.28
	x=5			
33.4027	461.77	0.2165	2.68261	100
35.7773	403.35	0.2558	2.50982	87.35
41.1243	108.58	0.2165	2.19501	23.51
49.7094	156.02	0.2362	1.83417	33.79
54.3154	202.2	0.2362	1.68902	43.79
57.1788	93.06	0.2362	1.61105	20.15
62.73	221.04	0.3149	1.48118	47.87
64.2442	111.05	0.3149	1.44988	24.05
72.3525	42.68	0.576	1.30499	9.24
	x=10			
32.926	218.75	0.2362	2.72035	91.3
35.2515	239.6	0.1968	2.54604	100
40.3052	28.22	0.9446	2.2377	11.78
49.3067	82.04	0.2362	1.84821	34.24
53.901	110.02	0.2362	1.70102	45.92
56.7459	70.18	0.2362	1.62231	29.29
62.3193	179.34	0.2165	1.48995	74.85
63.8392	70.92	0.576	1.45689	29.6
	x=15			
33.0549	118.56	0.2165	2.71003	57.93
35.3565	204.66	0.2165	2.53872	100
40.1605	59.14	0.3149	2.24543	28.89
49.4272	42.8	0.4723	1.84398	20.91
54.0264	77.76	0.2362	1.69737	37.99
56.8621	69.71	0.2362	1.61927	34.06
62.475	117.57	0.336	1.48538	57.45

Table 5: XRD data of annealing temperature 600 °C

	x=0			
Position [° 2 Th.]	Height [cts]	FWHM [° 2 Th.]	d-spacing (Å)	Rel. Int. [%]
33.5233	320.1	0.2362	2.67324	89.86
35.9435	356.23	0.3739	2.4986	100
41.2857	64.21	0.9446	2.1868	18.03
49.8193	124.35	0.3149	1.83038	34.91
54.4223	152.04	0.3149	1.68595	42.68
57.6942	28.29	0.9446	1.59788	7.94
62.8458	149.9	0.2755	1.47873	42.08
64.3898	86.79	0.576	1.44575	24.36
	x=5			
33.4243	442.32	0.2165	2.68093	100
35.8643	368.05	0.2165	2.50393	83.21
41.1135	93.49	0.2362	2.19556	21.14
43.3022	56.8	0.3149	2.08952	12.84
49.7511	171.15	0.2165	1.83273	38.69
54.3483	218.75	0.1968	1.68807	49.45
62.7117	194.39	0.3542	1.48157	43.95
64.2493	129.79	0.312	1.44858	29.34
	x=10			
33.3565	302	0.2165	2.68622	100
35.7463	274.28	0.3936	2.51193	90.82
41.0821	77.02	0.2362	2.19716	25.5
49.6754	114.44	0.3149	1.83535	37.89
54.2778	153.06	0.2755	1.6901	50.68
62.6717	178.54	0.2755	1.48242	59.12
64.1999	86.11	0.288	1.44957	28.51
	x=15			
33.3553	158.21	0.2362	2.68631	79.35
35.6584	199.39	0.2362	2.51792	100
40.7792	36.07	0.9446	2.21278	18.09
49.6346	45.46	0.9446	1.83676	22.8
54.2798	96.18	0.3936	1.69004	48.23
57.1545	55.79	0.4723	1.61168	27.98
62.6692	139.82	0.3149	1.48247	70.12
64.1647	57.99	0.576	1.45028	29.08

Table 6: XRD data of annealing temperature 650 °C

	x=0			
Position [° 2 Th.]	Height [cts]	FWHM [° 2 Th.]	d-spacing (Å)	Rel. Int. [%]
33.381	415.08	0.2362	2.68431	96.96
35.8168	428.08	0.2952	2.50715	100
41.1111	98.08	0.3149	2.19568	22.91
49.6939	146.59	0.3149	1.83471	34.24
54.3095	192.42	0.2755	1.68819	44.95
62.7103	177.73	0.2165	1.4816	41.52
64.2504	133.98	0.384	1.44855	31.3
	x=5			
33.3933	368.59	0.2362	2.68334	100
35.8303	322.15	0.2558	2.50623	87.4
41.0964	100.44	0.2362	2.19643	27.25
49.6977	161.63	0.2362	1.83458	43.85
54.3207	209.59	0.2165	1.68887	56.86
62.6854	193.63	0.1968	1.48213	52.53
64.2114	128.42	0.312	1.44934	34.84
	x=10			
33.3954	300.48	0.2165	2.68318	100
35.8415	231.72	0.2165	2.50547	77.12
41.1014	68.26	0.2362	2.19618	22.72
49.6816	133.52	0.1968	1.83514	44.43
54.3346	175.5	0.2165	1.68947	58.41
62.6997	162.15	0.2362	1.48182	53.96
64.235	105.45	0.384	1.44886	35.09
	x=15			
33.3406	340.45	0.2362	2.68746	100
35.786	262.32	0.3149	2.50923	77.05
41.0557	81.17	0.2165	2.19852	23.84
49.6399	135.71	0.1968	1.83658	39.86
54.2644	182.99	0.2558	1.69048	53.75
62.6588	158.9	0.2755	1.48269	46.67
64.1909	118.07	0.288	1.44975	34.68

Table 7: Room temperature (298 K) resistivity of the as prepared samples

A. Sample: $(Fe_{100-x}V_x)_{75}P_{15}C_{10}$ (x=0, 5, 10 and 15)

B. Sample Size: Length, $l=1.2\times10^{-2}$ m, Width, $w= 8 \times 10^{-4}$ m, Thickness, $t= 25 \times 10^{-6}$ m

H (Tesla)	$\rho(\Omega\text{-m})\times10^{-6}$ x=0	$\rho(\Omega\text{-m})\times10^{-6}$ x=5	$\rho(\Omega\text{-m})\times10^{-6}$ x=10	$\rho(\Omega\text{-m})\times10^{-6}$ x=15
0	1.471	1.623	1.913	2.059
0.024	1.512	1.654	1.925	2.098
0.056	1.556	1.715	1.945	2.132
0.075	1.568	1.731	1.953	2.145
0.145	1.587	1.75	1.964	2.143
0.218	1.58	1.746	1.964	2.145
0.289	1.585	1.755	1.964	2.15
0.362	1.591	1.755	1.964	2.153
0.432	1.591	1.76	1.967	2.164
0.501	1.591	1.764	1.972	2.177
0.570	1.595	1.772	1.975	2.186

Table 8: Normalized resistivity, ρ(T)/ρ(RT) for temperature (93-298)K of the as prepared samples

T (K)	ρ(T)/ρ(RT) (x=0)	ρ(T)/ρ(RT) (x=5)	ρ(T)/ρ(RT) (x=10)	ρ(T)/ρ(RT) (x=15)
93	0.832	0.633	1.144	1.688
113	0.836	0.643	1.108	1.546
133	0.828	0.664	1.086	1.444
157	0.817	0.733	1.067	1.367
173	0.825	0.785	1.048	1.279
193	0.811	0.862	1.047	1.174
213	0.811	0.899	1.037	1.115
233	0.826	0.910	1.033	1.076
253	0.860	0.963	1.021	1.055
273	0.924	0.982	1.006	1.032
298	0.999	0.999	1.000	1.000

Table 9: Magnetoresistance (MR) at 298K of the as prepared samples

H (Tesla)	x=0	x=5	x=10	x=15
0	0	0	0	0
0.024	2.35	2.88	2.66	3.05
0.056	4.35	5	5.55	5.46
0.076	4.73	5.8	6.26	6.72
0.145	4.92	6.06	6.65	7.04
0.218	5.14	6.09	7	7.4
0.298	5.2	6.13	7.15	7.65
0.362	5.47	6.37	7.53	7.8
0.432	5.7	6.76	7.77	8.13
0.501	5.92	7.12	8.16	8.55
0.570	6.35	7.65	9.18	9.3

Table 10: Hall resistivity measurement at 298 K of the as prepared samples

H (Tesla)	$\rho_H(\Omega\text{-m})\times10^{-8}$ x=0	$\rho_H(\Omega\text{-m})\times10^{-8}$ x=5	$\rho_H(\Omega\text{-m})\times10^{-8}$ x=10	$\rho_H(\Omega\text{-m})\times10^{-8}$ x=15
0	0	0	0	0
0.024	0.55	0.65	0.58	0.744
0.056	1.1	1.18	1.32	1.44
0.076	1.256	1.334	1.552	1.644
0.145	1.269	1.340	1.557	1.646
0.218	1.249	1.359	1.565	1.647
0.298	1.267	1.350	1.558	1.672
0.362	1.257	1.358	1.565	1.654
0.432	1.272	1.346	1.574	1.662
0.501	1.268	1.364	1.572	1.656
0.570	1.276	1.369	1.580	1.669

Table 11: Magnetization measurement at 298 K of the as prepared samples

H (kG)	M (emu/g) x=0	M (emu/g) x=5	M(emu/g) x=10	M (emu/g) x=15
0	5.25	3.25	1.25	0.99
0.112	44.25	23.25	13.80	6.25
0.169	65.13	34.6	20.40	10.80
0.237	91.15	46.96	29.67	14.80
0.296	118.03	59.04	35.47	18.88
0.357	135.86	69.36	40.28	22.52
0.423	150.28	81.36	48.54	25.62
0.496	154.28	90.4	54.72	29.22
0.557	154.28	98.68	58.44	31.23
0.621	154.28	104.22	63.72	33.22
0.69	154.28	106.96	66.81	34.72
0.755	154.28	108.72	68.44	37.60
0.828	154.28	108.72	69.28	38.82
0.899	154.28	108.72	69.98	39.41
0.96	154.28	108.72	69.98	40.20
1.036	154.28	108.72	69.98	40.20
1.103	154.28	108.72	69.98	40.20
1.172	154.28	108.72	69.98	40.20